Numerical simulation of injection moulding : non-isothermal non-Newtonian flow of polymers in complex geometries

Document Version:
Publisher's PDF, also known as Version of Record (includes final page, issue and volume numbers)

Please check the document version of this publication:

• A submitted manuscript is the version of the article upon submission and before peer-review. There can be important differences between the submitted version and the official published version of record. People interested in the research are advised to contact the author for the final version of the publication, or visit the DOI to the publisher's website.
• The final author version and the galley proof are versions of the publication after peer review.
• The final published version features the final layout of the paper including the volume, issue and page numbers.

[Link to publication](#)

NUMERICAL SIMULATION OF INJECTION MOULDING

non-isothermal non-Newtonian flow of
polymers in complex geometries

Cox Sitters

NUMERICAL SIMULATION OF INJECTION MOULDING

non-isothermal non-Newtonian flow of

polymers in complex geometries

PROEFSCHRIFT

ter verkrijging van de graad van doctor
aan de Technische Universiteit Eindhoven,
op gezag· van de Rector Magnificus,
Prof. Dr. F. N. Hooge, voor een commissie
aangewezen door het college van Dekanen,
in het openbaar te verdedigen op
dinsdag 23 februari 1988 om 16.00 uur

door

CORNELIUS WILHELMUS MARIA SITTERS

geboren op 13 november 1953 te Klundert

Contents

Abstract

Injection moulding of thermoplastic materials is an industrial pro-
cess that allows complex thin walled products to be manufactered in
one machine cycle, in large numbers and at low cost. Driven by the
development of new polymers, the demands on the product quality are
increasing continuously. Also, the variety of applications grows at
the cost of conventional production techniques. In order to compen-
sate for the shortcoming of experience, numerical tools are wanted,
in order to predict the influence of the important material param-
eters and process conditions on the final quality of the product.
From a physical point of view, the injection moulding process is
complex. This thesis is confined to the analysis of the filling
stage, injecting a polymer fluid into a complex mould, with a small
varying gap size. Due to (asymmetric) cooling of the mould, solidi-
fied layers grow from the walls of the cavity. The viscosity of the
polymer depends on temperature, shear rate and pressure. The specific
volume and other thermodynamic properties are temperature and pres-
sure dependent.
This work includes a number of new aspects. The mathematical basis is
formed by a general continuum approach, in which the solid-liquid
interface is described as a discontinuity surface. The convection of
heat in all directions is taken into account. A stable explicit flow
front tracing technique is proposed that can be applied for every
arbitrary complex configuration.
A number of numerical simulations is presented and compared with the
experimental and numerical data from literature. The front tracing
method supplies satisfactory results, which hold for the pressure and
the temperature fields too. In all the results obtained, the velocity
component in the direction of the channel height was set to zero,
because evaluating this component was inaccurate. Another problem is
the decreasing accuracy of the temperature calculation with increas-
ing injection times. A suggestion is made to overcome these problems.
Nevertheless the theory presented, offers the possibility to predict
the behaviour of polymers during the filling stage of the injection
moulding process with improved reliability.

List of symbols

$\dot{A}$ an overdot denotes the material time derivative

$\underset{\sim}{A}$ a tilde denotes a column

$\underline{A}$ an underscore denotes a matrix

$\vec{A}$ an arrow above the symbol denotes a vector

$\mathbb{A}$ a shadow bar denotes a tensor

$\mathbb{A}^d$ denotes the deviatoric part of a tensor

$\mathbb{A}^c$ denotes the conjugate of a tensor

$tr(A)$ denotes the trace of a tensor

$det(A)$ denotes the determinant of a tensor

$\vec{A}\cdot\vec{B}$ a centered dot denotes a dot product

$\vec{A}*\vec{B}$ a centered asterix denotes a cross product

$\vec{A}\ \vec{B}$ denotes a dyadic product

$\mathbb{A}:\mathbb{B}$ a colon denotes a double dot product

$\vec{\nabla}$ denotes the gradient operator

a, b   denote parts of a material volume

f, s   denotes the fluid and the solid phase, respectively

*   denotes a vector with respect to the midplane of the mould

$[A]_d$ denotes the jump in value of A across a discontinuity surface

z   denotes the component of a vector in the direction of the channel height

A   surface

B   boundary of a surface

c_p specific heat capacity at constant pressure

c_v specific heat capacity at constant volume

$\mathbb{D}$ deformation rate tensor

f   specific free energy

$\vec{f}$ specific body force

g   surface heat flux

h	specific enthalpy, total channel height
$\mathbb{L}$	velocity gradient tensor
n	power law constant
$\vec{n}$	unit normal
p	mechanical pressure
p_0	thermodynamical pressure
p_r	reference pressure
$\vec{q}$	heat flux vector
r	radiation density
s	specific entropy
$\vec{t}$	surface load, stress vector
T	absolute temperature
T_c	crystallization temperature
T_g	glass transition temperature
T_s	solidification temperature
$\vec{u}_d$	velocity of a discontinuity surface
$\vec{v}$	material velocity
V	volume
w	weight function
$\vec{x}$	position vector
z	coordinate in the direction of the channel height
α^-, α^+	position of the lower and upper solid-liquid interface
$\dot{\gamma}$	shear rate
Δ	difference between two values of a quantity
Γ	specific transition heat
ε	specific internal energy
η	shear viscosity
κ_T	isothermal compressibility
λ	heat conduction coefficient
μ	bulk viscosity
ν	specific volume
ρ	mass density
σ	Cauchy stress tensor
σ^e	extra stress tensor
$\underset{\sim}{\phi}$	column with interpolation functions

1   GENERAL INTRODUCTION

1.1   The increasing importance of injection moulding

Injection moulding is an important industrial process for the series
production of complex thin walled or small thermoplastic products.
The repeated use of a mould, in which the product is formed is spe-
cific for this process. Driven by the development of new polymers
with a superior quality, the tendency is present to manufacture very
accurate and/or heavily loaded products by injection moulding, which
formerly were made with other techniques. The quality requirements
become so high that the manufacturing experience becomes inadequate,
therefore, it is desirable now to develop numerical tools which at
least will estimate the influence of various material properties and
process conditions on the final quality of products. The injection
moulding process is complex from a physical point of view. This
investigation is confined to the analysis of the filling stage of the
process.

1.2   General description of the injection moulding process

As mentioned, injection moulding is an important industrial process.
In an extruder, the raw granulated material is heated until it
reaches the fluid phase. After mixing, in order to obtain a homoge-
neous melt, the material is injected at high speed into the cooled
mould.
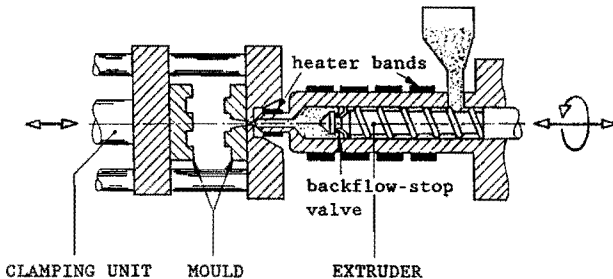
Fig. 1.2.1 The essential parts of a reciprocating screw injec-
tion moulding machine.

When the material is sufficiently solidified, a clamping unit opens
the mould and the product is ejected. Fig. 1.2.1 shows the essential
parts of a reciprocating screw injection moulding machine.
The extruder can be considered to be a rotating screw pump. The
polymer is melted by the frictional heat generated by the mechanical
deformation of the material and by heater bands which are fitted
around the cylinder of the extruder. During this plasticization
process, the molten homogenized material is transported to the end of
the screw, which moves slowly backwards to permit the polymer to
accumulate. When enough material has been plasticized, the screw is
forced forward acting as a plunger and the softened material is
injected into the cooled mould at high speed. A valve prevents the
backflow of the material, however, sometimes the flow resistance
along the screw channel is sufficient for this purpose.
After filling the mould, the full load on the screw causes the pres-
sure in the mould to rise to a maximum (compression). Some material
can still flow into the cavity in order to compensate for shrinkage
due to cooling (packing). When the gate seals, material can no longer
flow into the cavity and the product cools without compensation for
shrinkage. If the product is sufficiently solidified, the clamping
unit opens the mould and the product is ejected.
In summary, the following stages can be distinguished in the injec-
tion moulding process, as far as the mould is concerned:
- injection;
- packing;
- cooling;
- ejection.

1.3   The polymer during the process

A molten polymer can be considered to be a viscoelastic fluid, with
physical properties which depend on temperature and pressure. The
viscosity is high (100 - 10,000 Pas), consequently, high injection
pressures are required too (up to 100 Mpa).
In spite of the severe cooling of the mould (in order to reduce the
cycle time) it is possible to attain considerable flow lengths, this

can be explained by the low heat conductivity of the polymer, the
frictional heat developed during filling (keeping the polymer at a
reasonable high temperature), and reduced viscosity due to the high
shear rates (shear-thinning effect).
The cooling rates in a mould are high, especially, near the walls
where orientated solidified layers grow, accompanied by flow induced
stresses. Also, thermal stresses are created in these layers, because
shrinkage is prevented.
After the filling of the mould, the machine exerts high pressure on
the polymer. The relaxation time increases, caused by the high pres-
sure and the decreasing temperature. If the gate is sealed no further
compensation for volume is possible and the pressure in the mould
falls rapidly. When the product is ejected, it is no longer supported
by the mould and warpage and shrinkage of the product occurs, caused
by internal stresses. At that point, the rapid cooling ceases too.
The core of the product finally solidifies and the build up of resid-
ual stresses continues. Due to the initially rather high temperature,
the stresses will relaxate at the same time. During its life, the
product will be subjected to physical aging. In this period, the
product obtains its final mechanical and thermal properties and
dimensions.
From the description above, it can be concluded that the injection
moulding process is complex. The complete prediction of properties
and dimensions of a product is not possible presently although it is
desirable, because the demands made on moulded products are increas-
ing all the time. Within this respect has to be remarked too, that
the lack of experimental data for the material properties is evident,
therefore, a sucessful numerical simulation of the injection moulding
process requires:

- an extensive characterization of the material properties;
- well defined process conditions;
- an efficient numerical scheme to solve the set of non-linear equa-
  tions, which are derived from the balance equations, the constitu-
  tive equations and the initial and boundary conditions imposed by
  the mould and the process;

Well-defined experiments are necessary to verify the numerical model.

In the following Paragraph, a survey of the literature on this sub-
ject is presented. A course distinction can be made between analyti-
cal and numerical approaches.

1.4   Literature survey

The history of the attempt to solve the non-linear equations that
govern the flow of and the heat transfer in a molten thermoplastic
material passing through narrow cavities can be traced along four
main lines:
- analytical solutions of an integrated form of the equation for the
  heat transport;
- analytical approximations for the uni-directional flow, combined
  with heat transport, based on local balance equations;
- numerical solutions of the flow and the heat transport through
  simple cavities, based on the local balance equations;
- numerical analysis of the multi-directional flow and the heat
  transport through complex shaped cavities, based on local balance
  equations.
These lines are characterized by the level of approximation used, to
arrive at a set of equations that can be solved either by applied
mathematical tools (so-called analytical solutions) or numerical
techniques (finite difference and/or finite element approximations).

By using an integrated form of the equation for the conservation of
heat, information about local temperatures cannot be obtained, howev-
er, the equation of Janeschitz-Kriegl (1977, 1979) contains all the
phenomena which are relevant to the filing of a long duct with a
rectangular cross section.
To arrive at that equation Janeschitz-Kriegl splitted the computa-
tional domain into two parts, a part where the heat transport by
convection dominates and a part where the heat transport by conduc-
tion prevails. The heat generated by viscous dissipation is partly
removed by conduction through the nearly stagnant layers on to the
walls of the cavity. The remaining frictional heat flows to the core,
either undercompensating for the heat flow to the walls causing the

core temperature to decrease (slow flow), or overcompensating the heat flow to the walls causing the core temperature to rise (fast flow). Despite of the complex heat transfer problem, the core of the flow can be treated nearly isothermally. Then, the heat transfer problem can be solved with a standard Leveque approximation (Schlichting, 1982).

It appears that this approximation can be extended to include the so-called "power law" liquids. (Valstar and Beek, 1963; Bird, Armstrong and Hassager, 1987). In order to get the correct boundary conditions at the flow front, the "fountain flow" concept is used. This concept gives a rough approximation of the two-dimensional flow at the flow front, and showing that material flowing along the centre line flows to the wall (Tadmor, 1974). With the aid of this theory, it is possible to predict the shape of the solidified layer at the end of the filling stage. This has been confirmed by experiments done by Wales, Van Leeuwen and Van der Vijgh (1973), also see Wales (1976) and Janeschitz-Kriegl (1983).

Within this respect also the work in the same field of White (1975), Dietz, White and Clark (1978) and White and Dietz (1979) is relevant.

Starting with the full equations for the conservation of mass, momentum and energy in a liquid, flowing uni-directionally through a narrow slit, Pearson and Richardson describe a computational method based on precise examination of the type of flow and combined heat transfer problem that occurs at distinct places in the mould (1977, 1983, 1985, 1986). The flow and the heat transfer problems are catagorized by dimensionless numbers such as: Re, Na (Gr), Br, Pe (Gz). Each type of flow and associated heat transfer problem is governed by a set of equations containing only the most important terms, allowing in a number of cases to arrive at analytical closed form solutions. In this respect, attention should be paid to the analogous analysis in the papers of Martin (1967), Ockendon and Ockendon (1977), Ockendon (1979). Richardson, Pearson and Pearson (1980) described a computer program containing all the solutions previously mentioned, that can serve as a management tool for combining the outcomes in order to simulate flow during the filling of complex moulds. To do

so, the geometry of the mould has to be split into a number of stan-
dard conformations such as channels with either a circular, a square
or a rectangular cross-section. Moreover, a distinction has been made
between uni-directional parallel flow and uni-directional radial
flow.

The method proposed by Richardson, Pearson and Pearson has as a major
disadvantage, that it is difficult to choose the type of solution in
regions where the windows defined by the ranges of the dimensionless
numbers coincide or overlap. It is even difficult to define the exact
values of the dimensionless numbers where the solution changes type.
The advantage of the method is that even for complicated moulds,
filling can be simulated in a reasonably short calculation time.

In order to avoid the problem of looking for the right type of solu-
tion, it is more convenient to solve the set of equations containing
all relevant terms. This, of course, is at the expense of increased
computational time. In that case, methods are applied in adapted form
of the thin film theory, otherwise referred to as the lubrication
theory or Hele-Shaw theory (Richardson, 1972; Schmidt, 1976;
Schlichting, 1982). For uni-directional flow in simple cavities
(parallel and radial flow), the position of the flow front and,
consequently, the computational domain is completely known as a
function of the time. Because this domain has a simple shape it
appeared most convenient to solve the set of non-linear equations by
means of the finite difference method.

For parallel flow, Tadmor (1974), Williams and Lord (1975) and Lord
and Williams (1975) gave results based on the analytical solution of
the momentum equation and a solution of the energy equation by means
of a finite difference scheme. This method is improved by Van
Wijngaarden, Dijksman and Wesseling (1982) by taking into account the
transport of heat by convection in the direction of the channel
height. They used, as a starting point, the approximated energy
equation derived by Pearson (1977). Sitters and Dijksman (1986) and
Flaman and Dijksman (1986) also considered radial and conical flow
(either with respect to a cylindrical coordinate system or to a
toroidal coordinate system (Dijksman and Savenije, 1985)). The only

difference between parallel flow and the other flow types included in
the approximation, is that the average flow velocity is a function of
the coordinate in the direction of the flow, see also Laurencena and
Williams (1974) and Stevenson, Galskoy, Wang, Shen and Reber (1977).

When a multi-directional flow is considered, the complicating factors
are: determining the flow front as a function of time and the veloc-
ity distribution in the computational domain. As soon as the flow
field is known locally, the energy equation can be solved with nume-
rical techniques.
Some pioneering papers in this field are those of Hieber and Shen
(1980), Hieber, Socha, Shen, Wang and Isayev (1983) and Shen (1986).
In these papers, all the basics concerning the derivation of the
field equation and finite element formulation for the pressure, the
propagation of the flow front and the determination of the tempera-
ture field, including all relevant non-linearities, are present.
Since the computational domain expands as a function of the injection
time, the finite element mesh covering the fluid on the midplane of
the cavity has to be adapted at the same time. Together with the
solution of the pressure and the local velocity and temperature
field, this may require excessive computer time (Couniot, Crochet,
1986; Vanderschuren, Dupret, 1986; Iizuka, Gotoh, Miyamoto, Kubo,
Osaka, Sahara, 1986; Latrobe, De la Lande, Bung, preprint).
Modelling the flow of a molten polymer through a complicated cavity
may give rise to numerical instabilities (Hieber and Shen, 1980).
Pearson and Shah (1973), Pearson, Shah and Vieira (1973), Shah and
Pearson (1974) and Mhaskar, Shah and Pearson (1977) showed that
physical instabilities may occur too, during the non-isothermal flow
of a shear thinning liquid in a narrow cavity, even for parallel
flow.

1.5   Scope and framework of this thesis

The scope of this thesis is restricted to the injection of a polymer
into a complex three-dimensional cavity, with a small but varying gap
size. The viscosity of the polymer depends on temperature, shear rate

and pressure. Solidification of the polymer against the cooled walls
of the mould is taken into account. The solidification temperature is
pressure dependent and asymmetrical cooling is allowed. The specific
volume and the thermodynamic properties are temperature and pressure
dependent. For these properties, curve fits and/or tabulated ex-
perimental data can be used.

This research can be considered as an extension of the work of Hieber
and Shen (1980): solidification of polymer against the walls of the
mould, which can be cooled asymmetrically, is taken into account; a
free choice of the viscosity model is possible; the density of the
polymer is pressure and temperature dependent; material convection in
the direction of the channel height is taken into account.
In Chapter 2, balance equations for mass, momentum and energy are
derived for a material volume which is cut into two parts by a dis-
continuity surface. The reason for this approach is that the solid-
liquid interface can be regarded as such a surface, in principle
where, all quantities can change discontinuously. With the second law
of thermodynamics and the choice of a set of independent thermodynam-
ical variables, a frame is constructed for selecting the constitutive
equations.
In Chapter 3, the equations are simplified by combining geometrical
considerations with knowledge of the flow and temperature development
and distribution (thin film approximation).
In Chapter 4, attention is paid to the mechanical and thermodynamical
behaviours of polymers in general. Also, the adaptation of the mate-
rial curves, to make them suitable for numerical implementation, is
discussed.
In Chapter 5, the numerical process based on a mixed finite element/
finite difference method, is worked out. Within the thin film ap-
proximation the pressure appears to be independent of the coordinate
in the direction of the channel height. Therefore, it is sufficient
to evaluate the pressure at the midplane of the mould. This is done
with a finite element procedure in order to prevent problems due to
the complexity of the geometry of the midplane. The velocities and
the temperatures remain three-dimensional essentially and are solved

with a finite difference scheme. The finite difference grid lines are
applied in the direction of the channel height at the vertices of the
elements. The finite element mesh is spatially fixed and contains the
whole midplane of the cavity. The flow front moves through this fixed
mesh.

The problem is solved in a number of time increments. After each time
step, the new position of the flow front is calculated. At the flow
front, the mesh is adapted in such a manner that a proper mesh re-
sults. All the relevant equations are solved iteratively. After
convergence, a new time increment is made and the iteration cycle can
be repeated.

In Chapter 6, predictions of the flow fronts are compared with the
experimental results for a Newtonian fluid, between two parallel
plates. A number of simulations of injection in a centre gated disk
are carried out in order to investigate the influence of various
parameters. The injection of a strip is simulated and the results are
compared with the experimental and numerical results from literature.
Finally, filling a three-dimensional cavity with varying channel
height is simulated under realistic conditions. The predicted flow
fronts are compared to short shots made into an experimental mould of
similar dimensions.

Chapter 7 lists a number of problems which will have to be solved in
the future. Recommendations are made for the continuation of this
research.

2 FUNDAMENTAL EQUATIONS

2.1 Introduction

A heat conducting viscous fluid is considered as a continuum. The aim
is to predict, during a certain process, the density ρ, the velocity
$\vec{v}$ and the absolute temperature T in the fluid. For this purpose the
balance equations of mechanics and thermodynamics have to be solved,
after completion with constitutive equations, boundary and initial
conditions.

If solidification of the fluid occurs, the solid-liquid interface can
be described as a surface where, in principle, all quantities can
change discontinuously. Such a surface will be called a discontinuity
surface. Therefore, the jump relations at the discontinuity surface
with respect to the mechanics and the thermodynamics are important
too. The material in the solid phase will be regarded as a fluid with
a very high viscosity.

Because the use of discontinuity surfaces is not very common, the
local balance equations and jump relations will be derived with the
transport theorem for a material volume discussed in Appendix 1. Also
see Malvern (1969), Becker and Bürger (1975) and Müller (1985).

A material volume V(t), with surface A(t) and unit outward normal $\vec{n}$,
is cut into two parts $V^a(t)$ and $V^b(t)$, by a discontinuity surface
$A_d(t)$ with unit normal $\vec{n}_d$ pointing from $V^a(t)$ into $V^b(t)$ (Fig.2.1.1).
This discontinuity surface divides the surface A(t) into two parts
$A^a(t)$ and $A^b(t)$, such that the closure of $V^a(t)$ and $V^b(t)$ is given by
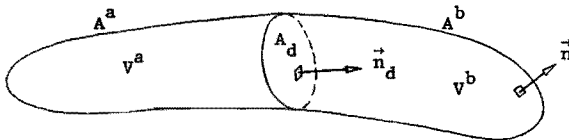the union of $A^a(t)$ and $A_d(t)$ and the union of $A^b(t)$ and $A_d(t)$, re-
spectively.

Fig. 2.1.1 Material volume, cut by a discontinuity surface.

A scalar or vector quantity $\phi(\vec{x},t)$ is considered, which is continuous and sufficiently differentiable in $V^a(t)$ and $V^b(t)$ and changes discontinuously at $A_d(t)$. The time derivative $\frac{d\Phi}{dt}$ of the integral $\Phi = \int\limits_V \phi dV$ can be written as (see A1.11)

$$\frac{d\Phi}{dt} = \int\limits_{V^a+V^b} (\dot{\phi} + \phi\vec{\nabla}\cdot\vec{v})dV - \int\limits_{A_d}[\phi(\vec{u}_d - \vec{v})]_d\cdot\vec{n}_d dA \qquad (2.1.1)$$

Here, the bracket notation $[\phi(\vec{u}_d - \vec{v})]_d$ with subscript d represents the difference $\phi^b(\vec{u}_d - \vec{v}^b) - \phi^a(\vec{u}_d - \vec{v}^a)$; this bracket notation will henceforth be used to indicate the jump in value of other quantities too. With $\dot{\phi}$, the material time derivative of ϕ is indicated. Further, the material velocity $\vec{v}$, the not material bounded velocity $\vec{u}_d$ of the discontinuity surface, as well as, the gradient operator $\vec{\nabla}$ are introduced. The velocity $\vec{v}$ of a certain particle is the material time derivative of its position $\vec{x}$ defined according: $\vec{v} = \dot{\vec{x}}$. The velocity $\vec{u}_d$ of the discontinuity surface is not uniquely defined. The normal component $\vec{u}_d\cdot\vec{n}_d$ however, which is relevant in (2.1.1), is a meaningful quantity.

After the balance equations, the entropy inequality resulting in the local Clausius Duhem inequality will be discussed. This inequality will be used in the next Paragraph, where the constitutive relations for the Cauchy stress tensor σ, the heat flux vector $\vec{q}$ and the internal energy ε are considered. Finally, the boundary and initial conditions will be considered in a very global manner.

2.2   Conservation of mass

The global equation for conservation of mass states that the mass in a material volume V does not change with time. In the case that V is cut into two parts by a discontinuity surface the balance equation reads

$$\frac{d}{dt}(\int\limits_{V^a+V^b} \rho dV) = 0 \qquad (2.2.1)$$

where ρ is the mass density. Using the transport theorem (2.1.1) it follows that

$$\int_{V^a+V^b} (\dot{\rho} + \rho\vec{\nabla}\cdot\vec{v})dV - \int_{A_d} [\rho(\vec{u}_d - \vec{v})]_d\cdot\vec{n}_d dA = 0 \qquad (2.2.2)$$

The equation above is valid for every V^a and V^b. Therefore, both integrands have to be equal to zero. This results in the local continuity equation and its jump relation

$$\dot{\rho} + \rho\vec{\nabla}\cdot\vec{v} = 0 \qquad \text{in } V^a \text{ and } V^b \qquad (2.2.3)$$

$$[\rho(\vec{u}_d - \vec{v})]_d\cdot\vec{n}_d = 0 \qquad \text{on } A_d \qquad (2.2.4)$$

2.3 Conservation of momentum

The global equation for conservation of momentum states that the rate of change of momentum for a material volume is equal to the resulting force of the applied external loads. The balance equation in the case that V is cut into two parts by a discontinuity surface reads

$$\frac{d}{dt}(\int_{V^a+V^b} \rho\vec{v}dV) = \int_{V^a+V^b} \rho\vec{f}dV + \int_{A^a+A^b} \vec{t}dA \qquad (2.3.1)$$

Here, $\vec{f}$ is the specific external body force and $\vec{t}$ the external surface load. Using the proposition of Cauchy, $\vec{t}$ can be replaced by $\sigma\cdot\vec{n}$, where σ is the Cauchy stress tensor and $\vec{n}$ the unit outward normal on A^a or A^b. Application of the transport theorem (2.1.1) and the theorem of Gauss leads using relation (2.2.3) to

$$\int_{V^a+V^b} (\rho\dot{\vec{v}} - \rho\vec{f} - \vec{\nabla}\cdot\sigma^c)dV - \int_{A_d} [\rho\vec{v}(\vec{u}_d - \vec{v}) + \sigma]_d\cdot\vec{n}_d dA = \vec{0} \qquad (2.3.2)$$

Requiring validity for every V^a and V^b, the relation above is equivalent to the local balance of momentum and its jump relation

$$\rho\dot{\vec{v}} - \rho\vec{f} - \vec{\nabla}\cdot\sigma^c = \vec{0} \qquad \text{in } V^a \text{ and } V^b \qquad (2.3.3)$$

$$[\rho\vec{v}(\vec{u}_d - \vec{v}) + \sigma]_d \cdot \vec{n}_d = \vec{0} \qquad \text{on } A_d \tag{2.3.4}$$

2.4 Conservation of moment of momentum

The global equation for conservation of moment of momentum states that the rate of change of moment of momentum of a material volume is equal to the resulting moments of the applied external loads. Volume and surface torques are not taken into account and therefore the balance equation can be written as

$$\frac{d}{dt}(\int_{V^a+V^b} \rho\vec{x}\!\ast\!\vec{v}dV) = \int_{V^a+V^b} \rho\vec{x}\!\ast\!\vec{f}dV + \int_{A^a+A^b} \vec{x}\!\ast\!\vec{t}dA \tag{2.4.1}$$

Again $\vec{t}$ can be replaced by $\sigma\cdot\vec{n}$. Applying the transport theorem (2.1.1), the theorem of Gauss and performing some mathematical manipulations, with relation (2.2.3), (2.3.3) and (2.3.4) leads to

$$\int_{V^a+V^b} (\sigma - \sigma^c)dV = 0 \tag{2.4.2}$$

Since this must hold for every V^a and V^b, this relation is equivalent to the local equation of moment of momentum according to

$$\sigma = \sigma^c \tag{2.4.3}$$

In this case, no relation for the discontinuity surface remains.

2.5 Conservation of energy (first law of thermodynamics)

The global equation for conservation of energy or the first law of thermodynamics states that the rate of change of the internal and kinetic energy of a material volume is equal to the mechanical power performed by the external loads and the supplied heat per unit of time. The formula reads

$$\frac{d}{dt}(\int_{V^a+V^b} (\rho\varepsilon + \frac{1}{2}\rho\vec{v}\cdot\vec{v})dV) =$$

$$\int_{V^a+V^b} \rho\vec{f}\cdot\vec{v}dV + \int_{A^a+A^b} \vec{t}\cdot\vec{v}dA + \int_{V^a+V^b} \rho r dV + \int_{A^a+A^b} g dA \qquad (2.5.1)$$

where ε is the specific internal energy, r is the specific radiation density absorbed by the body and g is the surface heat flux into the volume. The heat flux g can be replaced by $-\vec{q}\cdot\vec{n}$, where $\vec{q}$ is the heat flux vector. If $\vec{q}$ and $\vec{n}$ have opposite signs, heat will flow into the volume. In (2.5.1), $\vec{t}\cdot\vec{v}$ can be replaced by $(\sigma^c\cdot\vec{v})\cdot\vec{n}$. Application of the transport theorem (2.1.1) and the theorem of Gauss with relations (2.2.3), (2.3.3) and (2.4.3) leads to

$$\int_{V^a+V^b} (\rho\dot{\varepsilon} - \rho r - \sigma:D + \vec{\nabla}\cdot\vec{q})dV +$$

$$- \int_{A_d}[\rho(\varepsilon + \frac{1}{2}\vec{v}\cdot\vec{v})(\vec{u}_d - \vec{v}) + \sigma\cdot\vec{v} - \vec{q}]_d\cdot\vec{n}_d dA = 0 \qquad (2.5.2)$$

where the deformation rate tensor D is the symmetric part of the velocity gradient tensor $\vec{\nabla}\vec{v}$. Again, this equation is valid for every V^a and V^b and, therefore, equivalent to the local equation of energy and its jump relation

$$\rho\dot{\varepsilon} - \rho r - \sigma:D + \vec{\nabla}\cdot\vec{q} = 0 \qquad \text{in } V^a \text{ and } V^b \quad (2.5.3)$$

$$[\rho(\varepsilon + \frac{1}{2}\vec{v}\cdot\vec{v})(\vec{u}_d - \vec{v}) + \sigma\cdot\vec{v} - \vec{q}]_d\cdot\vec{n}_d = 0 \qquad \text{on } A_d \qquad (2.5.4)$$

2.6 Entropy inequality (second law of thermodynamics)

The second law of thermodynamics states that, in every thermo-mechanical process, the internal entropy production I in a material volume is equal to or greater than zero. The entropy production I equals the rate of change of the entropy of the volume, decreased by the heat supplied per time and divided by the absolute temperature T

$$I = \frac{d}{dt}(\int_{V^a+V^b} \rho s dV) - \int_{V^a+V^b} \frac{\rho r}{T} dV + \int_{A^a+A^b} \frac{\vec{q}\cdot\vec{n}}{T} dA \geqq 0 \qquad (2.6.1)$$

where s is the entropy density. This equation is known as the global Clausius Duhem inequality. Application of the transport theorem (2.1.1) and the theorem of Gauss with relations (2.2.3) and (2.5.3) leads to

$$\int_{V^a+V^b} (\rho\dot{s} - \frac{\rho\dot{\varepsilon}}{T} + \frac{\sigma:\mathbb{D}}{T} - \frac{\vec{q}\cdot\vec{\nabla}T}{T^2}) dV +$$

$$- \int_{A_d} [\rho s(\vec{u}_d - \vec{v}) - \frac{\vec{q}}{T}]_d \cdot \vec{n}_d dA \geqq 0 \qquad (2.6.2)$$

With this inequality valid for every V^a and V^b, follows the local entropy inequality (local Clausius Duhem inequality) and its jump relation

$$\rho T\dot{s} - \rho\dot{\varepsilon} + \sigma:\mathbb{D} - \frac{\vec{q}\cdot\vec{\nabla}T}{T} \geqq 0 \qquad \text{in } V^a \text{ and } V^b \qquad (2.6.3)$$

$$[\rho s(\vec{u}_d - \vec{v}) - \frac{\vec{q}}{T}]_d \cdot \vec{n}_d \leqq 0 \qquad \text{on } A_d \qquad (2.6.4)$$

2.7 Constitutive equations

In this Paragraph, the constitutive equations for σ and $\vec{q}$, and the elimination of $\dot{\varepsilon}$ from the energy equation, as well as, the relations at the solid-liquid interface will be discussed. The polymer will be described as a compressible heat conducting viscous fluid (Müller, 1985). Such a fluid can be characterized by the following set of independent variables ρ, L, T and $\vec{\nabla}T$, where L is the velocity gradient tensor $\vec{\nabla}\vec{v}$. Using the local continuity equation, the independent variable L can be replaced by the independent variables $\dot{\rho}$ and L^d, with L^d the deviatoric part of L.

Clausius Duhem inequality

 A process with a fluid characterized by these independent variables
has to be thermodynamically admissable. Therefore, the local Clausius
Duhem inequality (2.6.3) has to be satisfied.

It appears to be advantageous, to use the specific free energy f
instead of the specific internal energy ε. The specific free energy
is defined as

$$f = \varepsilon - Ts \qquad (2.7.1)$$

Due to the principle of equipresence, ε as well as s are functions of
the above mentioned set independent variables. Therefore, the specif-
ic free energy can be written as

$$f = f(\rho, \dot{\rho}, \mathbb{L}^d, T, \vec{\nabla}T) \qquad (2.7.2)$$

Using $\sigma : D = (\dot{\rho}/\rho)p + \sigma^d : \mathbb{L}^d$, where σ^d is the deviatoric part of σ and
$p = -\text{tr}(\sigma)/3$, (2.7.1) and (2.7.2) the local Clausius Duhem inequality
transforms into

$$\frac{1}{\rho}(p - \frac{\partial f}{\partial \rho}\rho^2)\dot{\rho} - \rho(\frac{\partial f}{\partial \dot{\rho}})\ddot{\rho} - \rho(\frac{\partial f}{\partial \mathbb{L}^d})^c : \dot{\mathbb{L}}^d - (\rho s + \rho\frac{\partial f}{\partial T})\dot{T} +$$

$$- \rho(\frac{\partial f}{\partial \vec{\nabla}T}) \cdot (\dot{\vec{\nabla}T}) + \sigma^d : \mathbb{L}^d - \frac{1}{T}\vec{q} \cdot \vec{\nabla}T \geq 0 \qquad (2.7.3)$$

In this expression $\ddot{\rho}$, $\dot{\mathbb{L}}^d$, $\dot{\vec{\nabla}T}$ and $\dot{T}$ can be varied independently,
therefore, the coefficients of these quantities have to be zero

$$\frac{\partial f}{\partial \dot{\rho}} = 0 \quad ; \quad \frac{\partial f}{\partial \mathbb{L}^d} = 0 \quad ; \quad \frac{\partial f}{\partial \vec{\nabla}T} = \vec{0} \qquad (2.7.4)$$

$$s = -\frac{\partial f}{\partial T} \qquad (2.7.5)$$

From (2.7.4), (2.7.5) and (2.7.1) it follows that f and ε are func-
tions of the independent variables ρ and T only, i.e.

$$f = f(\rho, T) \quad ; \quad \varepsilon = \varepsilon(\rho, T) \qquad (2.7.6)$$

Relation (2.7.3) reduces to

$$\frac{1}{\rho}(p - \frac{\partial f}{\partial \rho}\rho^2)\dot{\rho} + \sigma^d : \mathbb{L}^d - \frac{1}{T}\vec{q}\cdot\vec{\nabla}T \geqq 0 \tag{2.7.7}$$

Constitutive equations for σ and $\vec{q}$
The relation above can be simplified by using the following definitions

$$p = p(\rho,\dot{\rho},\mathbb{L}^d,T,\vec{\nabla}T) = p_0(\rho,T) + p_1(\rho,\dot{\rho},\mathbb{L}^d,T,\vec{\nabla}T) \tag{2.7.8}$$

$$p_0(\rho,T) = \frac{\partial f(\rho,T)}{\partial \rho}\rho^2 \tag{2.7.9}$$

where p_0 is called the thermodynamical pressure, depending on density
and temperature only. With the principle of equipresence, the Cauchy
stress tensor $\sigma = -p\mathbb{I} + \sigma^d$ can be written as

$$\sigma = - p_0(\rho,T)\mathbb{I} + \sigma^e(\rho,\dot{\rho},\mathbb{L}^d,T,\vec{\nabla}T) \quad ; \quad \sigma^e = - p_1\mathbb{I} + \sigma^d \tag{2.7.10}$$

where σ^e is called the extra stress tensor. Using the relations
(2.7.8), (2.7.9) and (2.7.10), the local Clausius Duhem inequality
reduces further to

$$\sigma^e : \mathbb{D} - \frac{1}{T} \vec{q}\cdot\vec{\nabla}T \geqq 0 \tag{2.7.11}$$

The constitutive equations for σ^e and $\vec{q}$ have to obey the principle of
objectivity. Therefore, $\mathbb{L}^d$ has to be replaced by its symmetric part,
the objective tensor $\mathbb{D}^d$. The temperature gradient $\vec{\nabla}T$ is objective.
For σ^e and $\vec{q}$ follows

$$\sigma^e = \sigma^e(\rho,\dot{\rho},\mathbb{D}^d,T,\vec{\nabla}T) \quad ; \quad \vec{q} = \vec{q}(\rho,\dot{\rho},\mathbb{D}^d,T,\vec{\nabla}T) \tag{2.7.12}$$

In fact, no further conclusions can be drawn from (2.7.11) and
(2.7.12). Therefore, constitutive laws for σ^e and $\vec{q}$ will be proposed
and checked afterwards with respect to (2.7.11). Isotropic constitu-
tive relations will be chosen of the following type

$$\sigma^e = \mu \mathrm{tr}(D) I + 2\eta D^d \quad ; \quad \mu = \mu(\rho, \dot{\rho}, I_2(D^d), I_3(D^d), T)$$

$$; \quad \eta = \eta(\rho, \dot{\rho}, I_2(D^d), I_3(D^d), T) \qquad (2.7.13)$$

$$\vec{q} = -\lambda \vec{\nabla} T \qquad ; \quad \lambda = \lambda(\rho, \dot{\rho}, I_2(D^d), I_3(D^d), T) \qquad (2.7.14)$$

Fluids that behave according to relation (2.7.13) will be called "generalized Newtonian fluids". The coefficients μ and η represent the bulk and shear viscosity, being a function of ρ, $\dot{\rho}$, T and the second and third invariant of D^d, defined by $I_2(D^d) = -\frac{1}{2}\mathrm{tr}(D^d \cdot D^d)$ and $I_3(D^d) = \frac{1}{3}\mathrm{tr}(D^d \cdot D^d \cdot D^d)$, respectively. Equation (2.7.14) is known as Fourier's law. The heat conductivity λ is a function of ρ, $\dot{\rho}$, T, $I_2(D^d)$ and $I_3(D^d)$ too. From the local Clausius Duhem inequality (2.7.11) it follows, with the assumption that both $\sigma^e{:}D$ and $-\vec{q}\cdot\vec{\nabla}T/T$ are non-negative, that the coefficients μ, η and λ have to be greater than or equal to zero.

Elimination of $\dot{\varepsilon}$ from the local energy equation

According to (2.7.6), the specific internal energy ε is only a function of ρ and T. Combining this with (2.2.3), (2.5.3) and (2.7.10) it follows that

$$\dot{\varepsilon} - \frac{p_0}{\rho^2}\dot{\rho} = c_v \dot{T} - \frac{T}{\rho^2}(\frac{\partial p_0}{\partial T})_\rho \dot{\rho} = r + \frac{1}{\rho}\sigma^e{:}D - \frac{1}{\rho}\vec{\nabla}\cdot\vec{q} \quad ;$$

$$c_v = (\frac{\partial \varepsilon}{\partial T})_\rho = c_v(\rho, T) \quad ; \quad p_0 = p_0(\rho, T) \qquad (2.7.15)$$

The quantity c_v is the specific heat capacity at constant density. Assuming that the relation for $p_0 = p_0(\rho, T)$ is invertible, p_0 and T can be considered as independent variables too, resulting in

$$\dot{\varepsilon} - \frac{p_0}{\rho^2}\dot{\rho} = c_p\dot{T} + \frac{T}{\rho^2}(\frac{\partial \rho}{\partial T})_{p_0}\dot{p}_0 = r + \frac{1}{\rho}\sigma^e{:}D - \frac{1}{\rho}\vec{\nabla}\cdot\vec{q} \quad ;$$

$$c_p = (\frac{\partial h}{\partial T})_{p_0} = c_p(p_0, T) \quad ; \quad \rho = \rho(p_0, T) \qquad (2.7.16)$$

The quantity c_p is the specific heat capacity at constant thermody-
namical pressure and is defined according to

$$c_p = (\frac{\partial h}{\partial T})_{p_0} \quad ; \quad h = \varepsilon + \frac{p_0}{\rho} \qquad (2.7.17)$$

where h is the specific enthalpy. The derivation of the expressions
above can be found in Appendix 2.
The energy equation according to (2.7.16) will be applied further on,
because in that case, if $p_0 \sim p$, experimental values for c_p can be
used.

Relations at the solid-liquid interface
Four relations at the solid-liquid interface are required, in order
to complete the set of equations. The jump in the specific internal
energy ε equals the specific phase transition heat Γ of the polymer.
The tangential velocities on both sides of this interface are equal.
Further, it will be assumed that the temperature is continuous across
the solid-liquid interface. This temperature equals the solidifica-
tion temperature T_s, which is the glass transition temperature for
amorphous polymers and the crystallization temperature for semi-
crystalline polymers. The relations are

$$[\varepsilon]_d + \Gamma = 0 \qquad (2.7.18)$$

$$[\vec{v} - \vec{v} \cdot \vec{n}_d \vec{n}_d]_d = \vec{0} \qquad (2.7.19)$$

$$[T]_d = 0 \qquad (2.7.20)$$

$$T - T_s = 0 \quad \text{on } A_d \qquad (2.7.21)$$

The effect of undercooling, which often occurs with semi-crystalline
polymers, is not taken into account. In that case, (2.7.21) has to be
replaced by a more complicated constitutive equation which couples
the normal velocity of the solid-liquid interface to the growth rate
of the crystals (Janeschitz-Kriegl, Krobath, Roth, Schausberger,
1983; Eder, Janeschitz-Kriegl, 1984; Janeschitz-Kriegl, Eder,

Krobath, Liedauer, 1987; Janeschitz-kriegl, Wimberger-Friedl,
Krobath, Liedauer, 1987).

From the discontinuity relation with respect to the entropy ine-
quality (2.6.4), it follows, as only result, that the jump in entropy
$[s]_d$ and the transition heat Γ have opposite signs.

2.8   Recapitulation

In the volumes V^a and V^b, the balance equations (2.2.3), (2.3.3),
(2.4.3) and (2.7.16) and the constitutive equations (2.7.10),
(2.7.13) and (2.7.14) are valid, i.e.

$$\dot{\rho} + \rho\,\mathrm{tr}(\mathbb{D}) = 0 \tag{2.8.1}$$

$$\rho\dot{\vec{v}} - \rho\vec{f} - \vec{\nabla}\cdot\sigma^c = \vec{0} \quad ; \quad \sigma = \sigma^c \tag{2.8.2}$$

$$\rho c_p\dot{T} + \frac{T}{\rho}(\frac{\partial\rho}{\partial T})_{p_0}\dot{p}_0 - \rho r - \sigma^e{:}\mathbb{D} + \vec{\nabla}\cdot\vec{q} = 0 \tag{2.8.3}$$

$$\sigma = - p_0 I + \sigma^e \quad ; \quad \sigma^e = \mu\,\mathrm{tr}(\mathbb{D})I + 2\eta\mathbb{D}^d \tag{2.8.4}$$

$$\vec{q} = - \lambda\vec{\nabla}T \tag{2.8.5}$$

where

$$\mu = \mu(p_0,\dot{\rho},I_2(\mathbb{D}^d),I_3(\mathbb{D}^d),T) \tag{2.8.6}$$

$$\eta = \eta(p_0,\dot{\rho},I_2(\mathbb{D}^d),I_3(\mathbb{D}^d),T) \tag{2.8.7}$$

$$\lambda = \lambda(p_0,\dot{\rho},I_2(\mathbb{D}^d),I_3(\mathbb{D}^d),T) \tag{2.8.8}$$

$$c_p = c_p(p_0,T) \tag{2.8.9}$$

$$\rho = \rho(p_0,T) \tag{2.8.10}$$

Equation (2.7.16) has been chosen instead of (2.7.15), because, if
$p_0 \sim p$, experimental data are available for c_p. The density ρ in this

case is a dependent variable of p_0 and T. Therefore, in equations
(2.8.6),(2.8.7) and (2.8.8), ρ has been replaced by p_0.
The unknowns in these relations are $\vec{v}$, σ, $\vec{q}$, p_0, T, μ, η, λ, c_p and
ρ. The number of unknowns (22) is equal to the total number of equations.
The jump relations (2.2.4), (2.3.4) and (2.5.4) on A_d can be rearranged in a more appropriate form (Appendix 3) according to

$$\rho^b(\vec{u}_d - \vec{v}^b)\cdot\vec{n}_d - \rho^a(\vec{u}_d - \vec{v}^a)\cdot\vec{n}_d = 0 \qquad (2.8.11)$$

$$(\vec{v}^b - \vec{v}^a)\rho^b(\vec{u}_d - \vec{v}^b)\cdot\vec{n}_d + (\sigma^b - \sigma^a)\cdot\vec{n}_d = \vec{0} \qquad (2.8.12)$$

$$(\varepsilon^b - \varepsilon^a)\rho^b(\vec{u}_d - \vec{v}^b)\cdot\vec{n}_d + (\vec{v}^b - \vec{v}^a)\cdot\frac{\sigma^b + \sigma^a}{2}\cdot\vec{n}_d +$$

$$- (\vec{q}^b - \vec{q}^a)\cdot\vec{n}_d = 0 \qquad (2.8.13)$$

The relations (2.7.18) - (2.7.21) on the solid-liquid interface are

$$\varepsilon^b - \varepsilon^a + \Gamma = 0 \qquad (2.8.14)$$

$$(\vec{v}^b - \vec{v}^b\cdot\vec{n}_d\vec{n}_d) - (\vec{v}^a - \vec{v}^a\cdot\vec{n}_d\vec{n}_d) = \vec{0} \qquad (2.8.15)$$

$$T^b - T^a = 0 \qquad (2.8.16)$$

$$T - T_s = 0 \quad \text{on } A_d \qquad (2.8.17)$$

The total number of equations (2.8.11) - (2.8.17) is 11, 10 transition relations are required for $\vec{v}$, $\sigma\cdot\vec{n}_d$, ε, $\vec{q}\cdot\vec{n}_d$, p_0 and T (the unknown ρ has been replaced by p_0 and T). An extra unknown is the normal velocity $\vec{u}_d\cdot\vec{n}_d$ of the discontinuity surface.
With sufficient initial and boundary conditions the solution of the problem can be determined in principle. These conditions at this stage will be discussed in a rather global manner. A detailed description of the conditions follows later. Three types of boundaries can be distinguished: the injection area(s), the walls of the mould

in contact with the polymer and the flow front. The following bound-
ary conditions have to be prescribed:

-at the injection area(s), the temperature of the injected material,
 as well as, the surface stress or the velocity;

-at the cooled walls, the temperature, or the heat flux and the
 velocity (no-slip);

-at the flow front, the heat flux and the surface stress.

Due to the non-linearity of the equations, the problem will be solved
in a number of time steps. The results from the previous time step
will be used as initial conditions. The first time step when the
mould is almost empty, a fair estimation of the initial conditions
can be made. In principle, the balance equations with jump relations,
constitutive equations, boundary and initial conditions can be solved
for a certain injection moulding problem.

3   THIN FILM APPROXIMATION

3.1   Introduction

In this Chapter, geometrical considerations are combined with flow
and temperature assumptions and used to simplify the governing equa-
tions. The result of this procedure is called the thin film or lubri-
cation approximation (Richardson, 1972; Schmidt, 1976; Schlichting,
1982). The point of departure is the complete set of equations men-
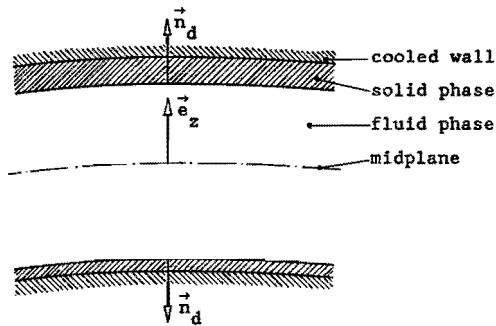tioned in Paragraph 2.8.

Fig. 3.1.1 The solid-liquid interfaces.

In the jump relations, however, the superscripts b and a are replaced
by s and f, respectively, denoting the solid and the fluid phases.
The unit normal vector at the solid-liquid interface points from the
liquid into the solid phase (Fig. 3.1.1).
In Paragraph 3.2 the characteristics of the geometry, the velocity
and the temperature fields are discussed. In Paragraph 3.3, the
governing equations for the liquid, as well as, the solid phase
including the jump relations, are simplified using the assumptions
made in Paragraph 3.2.
Within this approximation, the most important deductions are given
below.
-In the momentum equation, the inertial and gravity forces can be
 neglected with respect to the viscous forces (Re $\ll$ 1 and Re $\ll$ Fr).

- The coordinate in the direction of the channel height is not relevant in the remaining part of the momentum equation.
- In the solid phase no constitutive equation for σ is used, because the shear stress distribution can be calculated directly, from the momentum equation.
- In the core of the flow the velocities are high and the heat transport takes place mainly by convection (Pe >> 1). Close to the wall the velocities are low and the heat conduction to that wall dominates. In order to get a uniform description for the whole region, the heat convection, as well as, the heat conduction perpendicular to the wall, are taken into account.

3.2 Characteristics of the geometry, the velocity field and the temperature field

Geometry

The cavity is a three-dimensional weakly, curved channel. At the midplane of the channel, a unit normal $\vec{e}_z$ can be defined. In the direction of $\vec{e}_z$, a distance measuring coordinate z is chosen, which equals zero at the midplane.
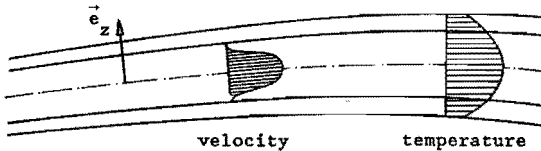

Fig. 3.2.1 Geometry, velocity field and temperature field.

An arbitrary vector $\vec{a}$ can be decomposed into a tangent vector $\vec{a}^{*}$, perpendicular to $\vec{e}_z$, and a normal vector $a_z \vec{e}_z$ in the direction of $\vec{e}_z$. The tangent vector is defined by

$$\vec{a}^{*} = \vec{a} - a_z \vec{e}_z \quad ; \quad a_z = \vec{a} \cdot \vec{e}_z \tag{3.2.1}$$

Similarly the (midplane) gradient operator $\vec{\nabla}^{*}$ can be defined as

$$\vec{\nabla}^* = \vec{\nabla} - \vec{e}_z \frac{\partial}{\partial z} \tag{3.2.2}$$

where $\vec{\nabla}$ is the usual gradient operator. It is assumed that $\vec{\nabla}^*$ is independent of the z coordinate, which only holds for weakly curved midplanes. As a result for tr(D) follows

$$tr(D) = \vec{\nabla}^* \cdot \vec{v}^* + \frac{\partial v_z}{\partial z} \tag{3.2.3}$$

The dimension of the channel in the z direction is small compared with the dimensions of the midplane. Further, the channel height is assumed to be a weakly varying function of the coordinates in the midplane (Fig. 3.2.1). This will be valid for the thickness of the solidified layers against the cooled walls too. Therefore, the unit normals $\vec{n}_d$ at the solid-liquid interfaces, with a good approximation, can be written as

$$\vec{n}_d = \vec{e}_z \quad ; \quad \vec{n}_d = - \vec{e}_z \tag{3.2.4}$$

for the upper and the lower interface, respectively.

Velocity field and temperature field in the fluid domain
Due to the shape of the cavity and the no-slip condition at the walls the velocity gradients in the z direction are very large, compared to the gradients parallel to the midplane. Also, the z component of the velocity is small, compared to the component in the flow direction. Therefore, the deviatoric part D^d of the deformation rate tensor can be approximated by

$$D^d = \frac{1}{2} \frac{\partial}{\partial z} (\vec{v}^* \vec{e}_z + \vec{e}_z \vec{v}^*) \tag{3.2.5}$$

Also holds

$$(tr(D))^2 << D^d : D^d \tag{3«2.6}$$

Combining (3.2.5) with the constitutive equation (2.8.4) it can be seen that the stress tensor $2\eta\mathbb{D}^d = \sigma^e - \mu tr(\mathbb{D})\mathbb{I}$ can be interpretated as a shear stress tensor.

Due to the severe cooling of the mould, combined with a huge heat convection in the flow direction (Pe $\gg$ 1), the temperature gradients in the z direction are very large, compared to the gradients parallel to the midplane. Furthermore, the temperature gradient vector can be approximated by

$$\vec{\nabla}T = \frac{\partial T}{\partial z}\vec{e}_z \tag{3.2.7}$$

Velocity field and temperature field in the solid domain

The density ρ is not constant and hence $\dot{\rho} = -\rho(\vec{\nabla}\cdot\vec{v})$ will be unequal to zero. Therefore, a material velocity has to be present in the solid region. Assuming that this velocity has a component in the direction of $\vec{n}_d$ only, using (3.2.4) it can be written as

$$\vec{v} = v_z\vec{e}_z \tag{3.2.8}$$

This velocity component is important in the jump relations with respect to the solid-liquid interface.

For the temperature gradient vector the approximation (3.2.7) is valid again

$$\vec{\nabla}T = \frac{\partial T}{\partial z}\vec{e}_z \tag{3.2.9}$$

3.3 Simplification of the governing equations

Constitutive equations

The bulk viscosity μ and the shear viscosity η are of the same order of magnitude. Therefore, in the constitutive equation (2.8.4), because of relation (3.2.6), the term $\mu tr(\mathbb{D})I$ can be neglected with respect to the term $2\eta\mathbb{D}^d$. The constitutive relation for σ in the fluid phase reduces to

$$\sigma = -p\mathbb{I} + \sigma^e \quad ; \quad \sigma^e = 2\eta\mathbb{D}^d \tag{3.3.1}$$

with D^d according to (3.2.5). Here is used already that now the hydrostatic pressure $p = -\frac{1}{3}tr(\sigma)$ and the thermodynamical pressure p_0 are equal

$$p = p_0 \tag{3.3.2}$$

In the solid phase, no constitutive equation for σ is used. Later will be shown that employing extra assumptions, the shear stresses directly can be determined from the momentum equation.
The constitutive relation (2.8.5) for $\vec{q}$ in the solid as well as the liquid domains, using (3.2.7) or (3.2.9), reduces to

$$\vec{q} = -\lambda\frac{\partial T}{\partial z}\vec{e}_z \tag{3.3.3}$$

Balance equations in the fluid phase
The continuity equation (2.8.1) transforms, with (3.2.3), into

$$\vec{\nabla}^*\cdot\vec{v}^* + \frac{\partial v_z}{\partial z} = -\frac{\dot{\rho}}{\rho} \tag{3.3.4}$$

From estimations it is known that the very high viscosity of the polymer make the inertial and gravity forces negligible with respect to the viscous forces (Re $\ll$ 1 and Re $\ll$ Fr). The momentum equation (2.8.2) reduces to

$$\vec{\nabla}^*p + \frac{\partial p}{\partial z}\vec{e}_z = \vec{\nabla}^*\cdot\sigma^d + \frac{\partial \sigma^d}{\partial z}\cdot\vec{e}_z \tag{3.3.5}$$

To elaborate this equation, the constitutive relation for σ (3.3.1) will be substituted

$$\vec{\nabla}^*p + \frac{\partial p}{\partial z}\vec{e}_z = 2\vec{\nabla}^*\cdot(\eta D^d) + \frac{\partial}{\partial z}(\eta D^d)\cdot\vec{e}_z \tag{3.3.6}$$

With D^d according to (3.2.5) this result can be rewritten as

$$\vec{\nabla}^*p = \frac{\partial}{\partial z}(\eta\frac{\partial \vec{v}^*}{\partial z}) \tag{3.3.7}$$

$$\frac{\partial p}{\partial z} = 0 \tag{3.3.8}$$

Substituting the constitutive equation (3.3.1) for σ^e and (3.3.3) for $\vec{q}$ in the energy equation (2.8.3), and neglecting the radiation density, produces

$$\rho c_p \dot{T} = \frac{\partial}{\partial z}(\lambda \frac{\partial T}{\partial z}) + \eta \dot{\gamma}^2 - \frac{T}{\rho}(\frac{\partial \rho}{\partial T})_p \dot{p} \tag{3.3.9}$$

where the shear rate $\dot{\gamma}$ has been defined by

$$\dot{\gamma} = \text{sqrt}(2\mathbb{D}^d : \mathbb{D}^d) \tag{3.3.10}$$

Substitution of the relation for $\mathbb{D}^d$ (3.2.5) in this equation leads to

$$\dot{\gamma} = |\frac{\partial \vec{v}^*}{\partial z}| \tag{3.3.11}$$

Balance equations in the solid phase

The continuity equation, using (3.2.8), can be written as

$$\frac{\partial v_z}{\partial z} = -\frac{\dot{\rho}}{\rho} \tag{3.3.12}$$

From equation (3.3.8), it follows that in the fluid domain the pressure is independent of the z coordinate. It will be assumed that, in the solidified layer, the pressure in the z direction is constant too, i.e.

$$\frac{\partial p}{\partial z} = 0 \tag{3.3.13}$$

In the energy equation, the term $\sigma^e : D$ is neglected, since the energy dissipation due to mechanical deformation is very small in the solid phase. With the constitutive equation for $\vec{q}$, the energy equation, neglecting the radiation term, becomes

$$\rho c_p \dot{T} = \frac{\partial}{\partial z}(\lambda \frac{\partial T}{\partial z}) - \frac{T}{\rho}(\frac{\partial \rho}{\partial T})_p \dot{p} \tag{3.3.14}$$

Jump relations

The jump relation for the continuity equation (2.8.11), using (3.2.4) becomes

$$\rho^s(u_z - v_z^s) - \rho^f(u_z - v_z^f) = 0 \qquad (3.3.15)$$

where u_z and v_z are the components of $\vec{u}_d$ and $\vec{v}$ in the z direction, respectively. Substituting the relation (2.8.15) in the jump relation for the momentum equation (2.8.12), and using (2.8.11) leads to

$$\frac{\rho^s - \rho^f}{\rho^s \rho^f}[\rho^s(u_z - v_z^s)]^2 \vec{n}_d + (\sigma^s - \sigma^f)\cdot\vec{n}_d = \vec{0} \qquad (3.3.16)$$

From the equaion above it can be concluded, that $\vec{n}_d \cdot \sigma \cdot \vec{n}_d$ is discontinuous. However, under practical circumstances, the absolute value of $\vec{n}_d \cdot \sigma^s \cdot \vec{n}_d$ or $\vec{n}_d \cdot \sigma^f \cdot \vec{n}_d$ is more than a factor 10^{10} larger than the discontinuity in the stress. Therefore, with a very good approximation, using (3.2.4), the jump relation for the momentum equation simplifies to

$$(\sigma^s - \sigma^f)\cdot\vec{e}_z = \vec{0} \qquad (3.3.17)$$

The jump relation for the energy equation (2.8.13) with the aid of (2.8.11), (3.3.17), the constitutive relations for σ (3.3.1) and $\vec{q}$ (3.3.3), and the relations for the discontinuity surface according (2.8.14) and (2.8.15) reduces to

$$(\Gamma + \frac{\rho^s - \rho^f}{\rho^s \rho^f}p)\rho^s(u_z - v_z^s) - \lambda^s(\frac{\partial T}{\partial z})^s + \lambda^f(\frac{\partial T}{\partial z})^f = 0 \qquad (3.3.18)$$

Shear stress distribution over the channel height

From the expressions for the momentum equations (3.3.8) and (3.3.13) and the jump relation (3.3.17), it can be concluded, that the pressure is constant over the full channel height. Once the pressure distribution is known (solution of 3.3.7), the shear stress distribution can be calculated from the momentum equation (3.3.5) if $\vec{\nabla}^* \cdot \sigma^d$ is neglected.
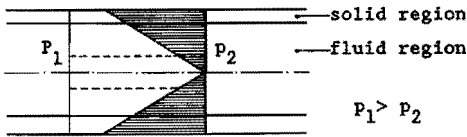
Fig. 3.3.1 Shear stress distribution.

The shear stress appears to be a linear function of the z coordinate. This, can be deduced from the equilibrium of forces on a slab of material parallel to the midplane too.

3.4 Recapitulation

The state of the polymer in the mould is completely determined, if the velocity, pressure and temperature fields, as well as, the velocity of the solid-liquid interfaces are known.

The nine unknowns in the fluid phase are $\vec{v}^*$, v_z, p, T, η, λ, c_p and ρ. The nine equations available are (3.3.4), (3.3.7) - (3.3.9) and (2.8.7) - (2.8.10).

In the solid phase, the following six unknowns have to be determined v_z, p, T, λ, c_p and ρ. The six equations available are given in (3.3.12) - (3.3.14) and (2.8.8) - (2.8.10).

The unknown at the discontinuity surface is the velocity u_z. Furthermore 6 transition relations are required for $\vec{v}^*$, v_z, p, $\partial T/\partial z$ and T (the unknown ρ has been replaced by p and T). The 7 available equations are (3.3.15), (3.3.17) (only necessary is: $(\sigma^s - \sigma^f):\vec{e}_z\vec{e}_z = p^s - p^f = 0$), (3.3.18), (2.8.15) and (2.8.16).

The velocity $\vec{v}^*$ in the solid phase is equal to zero, because of relation (3.2.8) and, therefore, does not belong to the unknowns. With the initial and boundary conditions, the problem can be solved in principle. A detailed specification of these conditions will be given later.

4   MATERIAL BEHAVIOUR

4.1   Introduction

In this Chapter, the material properties are discussed as functions
of the relevant variables. In the Paragraphs 4.2-4.5, the shear
viscosity η, the mass density ρ, the heat conduction coefficient λ
and the heat capacity c_p are characterized, respectively. Also,
attention will be paid to the determination of the solidification
temperature T_s and the specific transition heat Γ. The volume vis-
cosity μ is not important anymore within the thin film approximation.
According to the thermodynamic approach of Chapter 2, the choice is
a viscous, compressible, heat conducting fluid. Further, it is as-
sumed that the material behaves isotropically from mechanical and
thermal points of view. Therefore, theoretically, a number of impor-
tant effects will be excluded. Some of these effects are: elastic
stresses, orientation and birefringence, anisotropic heat conduc-
tivity, mass density dependent on the temperature history (free
volume). Of course, it is possible to deal with a number of these
effects in the computer program, however, with the consequence, it
does not fit in the thermodynamic framework chosen in Chapter 2.
Further can be remarked that the lack of experimental data is evi-
dent. For example, bearly no information about p-ν-T diagrams, mea-
sured at high cooling rates, and about the pressure dependence of the
thermodynamic properties is available. Also the influence of the
orientation on the heat conduction coefficient asks for more investi-
gation.

4.2   Shear viscosity

The dependence of shear viscosity (further, referred to as viscosity)
on shear rate (second invariant of D) and temperature is important.
Also, the effect of the pressure is considerable. The dependence on $\dot{\rho}$
and third invariant of D will be neglected. Fig. 4.2.1 shows what can
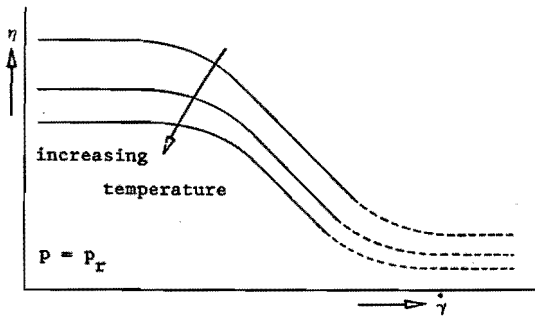be expected globally, for a constant pressure p_r.

Fig. 4.2.1 Shear viscosity as a function of shear rate and
temperature.

At low shear rates, the polymer behaves like a Newtonian fluid. At
higher shear rates, most polymers show a large decrease in viscosity,
the so-called shear-thinning effect. This experimental observation is
explained, as a result from the orientation of the molecules in the
direction of the flow. When the orientation is completed no further
shear-thinning is possible and the Newtonian behaviour returns. This
last part of the viscosity function is of no interest for the injec-
tion moulding process.
The data that is available concerning the shear rate dependence of
viscosity, covers the whole injection moulding field. However, there
is a lack of data about the temperature dependence, near the solidi-
fication temperature. Therefore, an extrapolation has to be made. At
low shear rates and at constant pressure, viscosity as a function of
the temperature, can be often approximated by the Arrhenius equation

$$\eta = B \exp(A/T) \quad ; \quad A \text{ and } B \text{ are constants} \tag{4.2.1}$$

An improved relation, to describe the dependence on temperature more
accurately, is the so-called WLF equation. In literature an extensive
treatise can be found (Ferry, 1980). Data for the pressure dependence
of viscosity are rather scarce (Cogswell, 1981). In most cases, it is

sufficient to enlarge the viscosity by a factor which depends on the pressure, i.e.

$$\eta(p,T,\dot{\gamma}) = \exp(\frac{p-p_r}{\beta})\eta(p_r,T,\dot{\gamma}) \qquad (4.2.2)$$

where p_r is a reference pressure.

It can be stated that the computer program which is developed can deal with the tabulated experimental viscosity data, completed with the temperature and pressure extrapolations. Nevertheless, curve fits such as the power law and the Carreau model can be used too. Examples of a five-parameter Carreau model and a three-parameter power law model, respectively, are given by

$$\eta = B_1\exp(A_1/T)[1 + (B_2\exp(A_2/T)\dot{\gamma})^2]^{(n-1)/2} \qquad (4.2.3)$$

$$\eta = B_1\exp(A_1/T)\dot{\gamma}^{n-1} \qquad (4.2.4)$$

where n is called the power law exponent; A_1, B_1, A_2 and B_2 are constants. It is noted that in these relations η is not a function of the pressure p.

4.3 Mass density or specific volume

The specific volume $\nu = 1/\rho$ as a function of the pressure p and the temperature T is usually represented in the p-ν-T diagram. such diagrams are available for low cooling rates (2-8 K/s). The behaviour of amorphous and semi-crystalline polymers is quite different (Fig. 4.3.1). If an amorphous polymer is cooled from the liquid phase, the specific volume will reduce more of less linearly with temperature. After a transition region the solid (glass) phase is reached and linearity returns, however, with different slope. The temperature at the intersection of the two tangent lines to the curves in the solid and the liquid phase, is called the glass transition temperature. Semi-crystalline polymers have a specific crystallization temperature T_c. In the liquid phase the behaviour is almost linear.
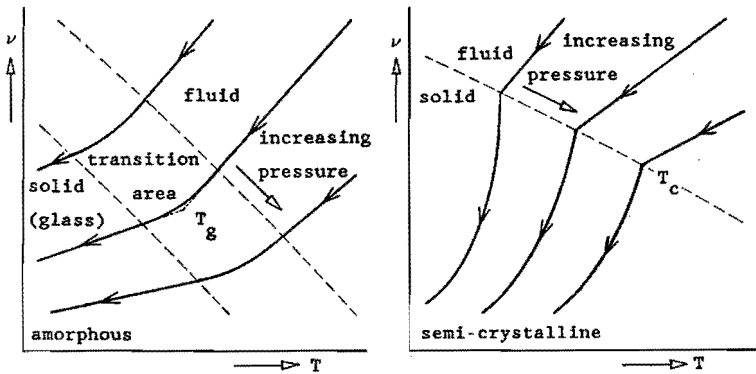
Fig. 4.3.1 p-ν-T diagrams for amorphous and semi-crystalline
polymers, at low cooling rates.

At the crystallization temperature, a sudden reduction of the specif-
ic volume occurs, resulting from the higher packing density in the
crystallized regions.
At high cooling rates, like those of the injection moulding process,
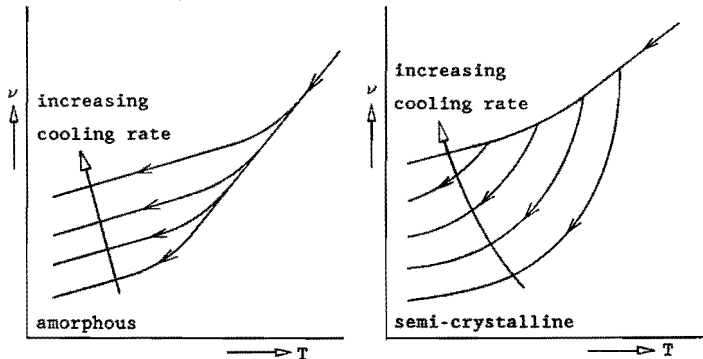the behaviour is quite different (Fig. 4.3.2).

Fig. 4.3.2 Diagrams for amorphous and semi-crystalline polymers
at different cooling rates, for a constant pressure.

The specific volume, due to the frozen free volume, will be higher
for increasing cooling rates. As a consequence the glass transition
temperature for amorphous polymers will shift to a higher temperature
(Ferry, 1980). The crystallization temperature for semi-crystalline
polymers shifts to a lower temperature (undercooling) or even may
vanish completely.
Data for the specific volume as a function of the cooling rate are
very scarce or not available at all.
The effect of cooling rate, or more general, the temperature history
is not incorporated in the thermodynamical model of Chapter 2. Within
this approach, the mass density only can be a function of the pres-
sure and temperature (2.7.16). Therefore the relevant p-ν-T diagrams
have to be applied, which are valid for a cooling rate which is
representative for the injection moulding process.
In Fig. 4.3.3, some possible curves which can be provided to the
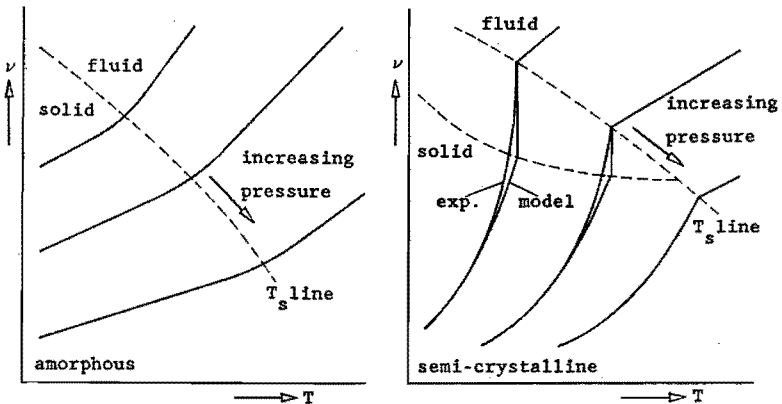computer program, have been drawn.

Fig. 4.3.3 p-v-T diagrams for amorphous and semi-crystalline
polymers, suitable to take into account.

From now on, the glass transition temperature T_g and the crystal-
lization temperature T_c will be referred to as T_s (solidification
temperature). From the p-ν-T diagram, it can be deduced that the

solidification temperature is approximately a linear function of
pressure.

If ν decreases suddenly during the cooling process, which occurs at
T_s for semi-crystalline polymers, it is advisable to introduce a jump
in ν at T_s. With a discontinuity surface between the solid and the
liquid region, this jump can be handled effectively.

4.4   Heat conduction coefficient

The heat conduction of a polymer molecule in the direction of the
backbone differs from the heat conduction perpendicular to that
direction, in general. If a certain amount of flow induced orienta-
tion is present in the polymer, the effective heat conduction coeffi-
cient λ will be dependent on the direction of the flow.
During the injection moulding process, a definite strong orientation
can be induced in the polymer, more or less parallel to the midplane
of the mould. In the mathematical model, presented in Chapter 2, an
isotropic constitutive relation for $\vec{q}$ has been postulated. Conse-
quently, the heat conduction is governed by scalar quantity (λ),
which is independent of direction.
Within the lubrication approximation, the heat conduction is accepted
to take place perpendicular to the midplane of the mould. Therefore,
the heat conduction coefficient perpendicular to the midplane, i.e.
perpendicular to the direction of the orientation will be chosen.
Apart from that, experimental data for λ as function of the orienta-
tion are very scarce (Knappe, 1976).
Further, it will be assumed that despite (2.8.8), the function λ,
used in actual calculations, depends on the pressure and temperature
only. However, only data measured under atmospheric conditions are
available. Fig. 4.4.1 shows a possible curve for λ perpendicular to
the direction of the orientation versus T measured under atmospheric
conditions. To approximate the influence of the pressure it is noted
that, at higher pressures the solidification temperature T_s in-
creases. In order to obtain a curve for λ at higher pressures, the
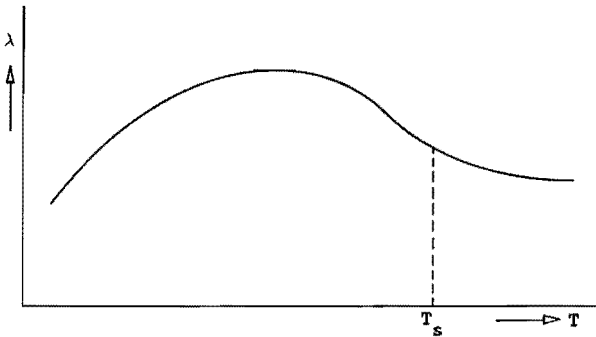same temperature shift will be applied to the complete curve shown in
Fig. 4.4.1.

Fig. 4.4.1 Heat conduction coefficient λ as a function of
temperature

4.5 Heat capacity at constant pressure and transition heat

In general, the heat capacity c_p will be measured with a differential
scanning calorimeter (DSC). These measurements usually take place
under atmospheric conditions and for low cooling rates. In Fig. 4.5.1
two measurements of the same sample are shown. Heating supplies the
endothermal curve and cooling the exothermal one. For the injection
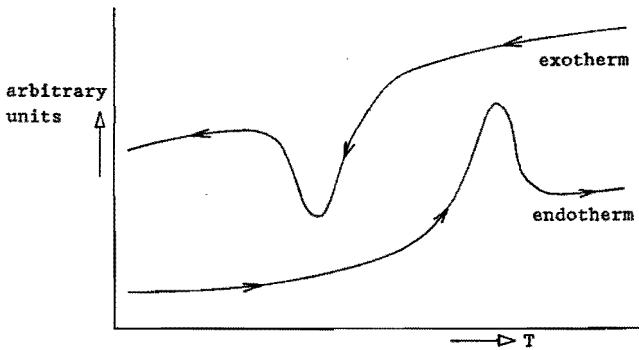moulding process the exothermal curve is of interest.

Fig. 4.5.1 Measurements for c_p with a differential scanning
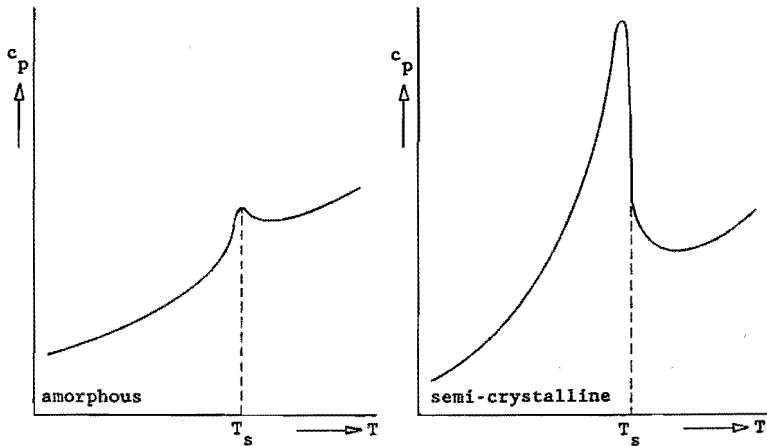calorimeter.

Fig. 4.5.2 Heat capacity for amorphous and semi-crystalline
          polymers.

Possible curves of c_p versus T for amorphous as well as semi-crystal-
line polymers are drawn in Fig. 4.5.2.
In a substantial part of the temperature range of interest, an impor-
tant contribution to c_p is delivered by the phase transition. For
semi-crystalline polymers, the value of c_p changes rapidly with
varying T near the crystallization temperature, because at this
temperature, most of the crystallization occurs.
The heat capacity c_p will be a function of the cooling rate too, for
instance, because of the shift of the glass transition temperature
and the crystallization temperature (Fig. 4.3.2). Also, the shape of
the curve will change: if a semi-crystalline polymer is cooled at
such a speed, the crystallization temperature vanishes, the peak in
c_p diminishes. The effects of the cooling rate mentioned are not
incorporated in the thermodynamic model of Chapter 2. Only the pres-
sure and temperature dependence of c_p (2.8.9) can be taken into
account. Therefore, those c_p curves have to be applied, that belong
to a cooling rate which is characteristic for the injection moulding
process.

The pressure dependence of c_p will be calculated completely analogously to the pressure dependence of λ as discussed in Paragraph 4.4. If the slope of the curve, representing c_p as a function of T, reaches high values (semi-crystalline polymers), a moderating procedure is applied (Fig. 4.5.3).
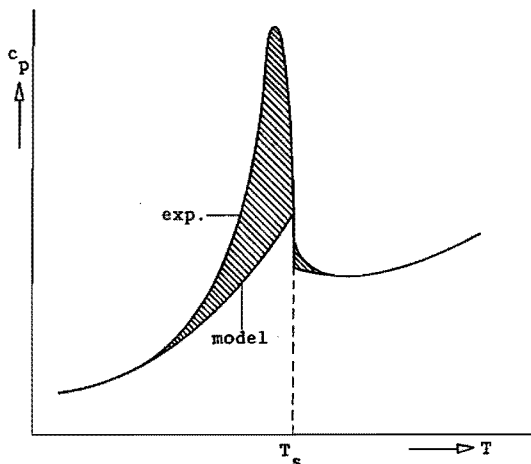

Fig. 4.5.3 Adaptation of the c_p curve, suitable to take into account.

The shaded part can be related to the transition heat, $\Gamma = \varepsilon^f - \varepsilon^s$, which is released instantaneously at the solidification temperature T_s (Stefan formulation: Carslaw and Jaeger, 1959; Hill, 1987). From relation (2.7.15) it can be derived, that the infinitesimal change in specific internal energy $d\varepsilon$, equals $c_v dT$, at constant density. Assuming that there is no difference between c_p and also c_v (A2.11), for the original and the adapted curves, respectively, within a good approximation can be derived

$$\Gamma = \int_T (c_p - c_p^*) dT \qquad (4.5.1)$$

where c_p and c_p^* indicate the original and adapted curves, respectively. The transition heat is equal to the shaded area in Fig. 4.5.3.

5   NUMERICAL PROCEDURE

5.1   Introduction

In this chapter the numerical solution of the equations, resulting
after the thin film approximation of Chapter 3, will be discussed.
The relevant balance equations derived, will be repeated first.
In the fluid phase

$$\vec{\nabla} \cdot \vec{v}^* + \frac{\partial v_z}{\partial z} = - \frac{\dot{\rho}}{\rho} \tag{5.1.1}$$

$$\vec{\nabla}^* p = \frac{\partial}{\partial z}(\eta \frac{\partial \vec{v}^*}{\partial z}) \quad ; \quad \frac{\partial p}{\partial z} = 0 \tag{5.1.2}$$

$$\rho c_p \dot{T} = \frac{\partial}{\partial z}(\lambda \frac{\partial T}{\partial z}) + \eta \dot{\gamma}^2 - \frac{T}{\rho}(\frac{\partial \rho}{\partial T})_p \dot{p} \tag{5.1.3}$$

with

$$\dot{\gamma} = |\frac{\partial \vec{v}^*}{\partial z}| \tag{5.1.4}$$

In the solid phase

$$\frac{\partial v_z}{\partial z} = - \frac{\dot{\rho}}{\rho} \tag{5.1.5}$$

$$\frac{\partial p}{\partial z} = 0 \tag{5.1.6}$$

$$\rho c_p \dot{T} = \frac{\partial}{\partial z}(\lambda \frac{\partial T}{\partial z}) - \frac{T}{\rho}(\frac{\partial \rho}{\partial T})_p \dot{p} \tag{5.1.7}$$

On the solid-liquid interface

$$\rho^s(u_z - v_z^s) - \rho^f(u_z - v_z^f) = 0 \tag{5.1.8}$$

$$p^s - p^f = 0 \tag{5.1.9}$$

$$(\Gamma + \frac{\rho^s - \rho^f}{\rho^s \rho^f}p)\rho^s(u_z - v_z^s) - \lambda^s(\frac{\partial T}{\partial z})^s + \lambda^f(\frac{\partial T}{\partial z})^f = 0 \tag{5.1.10}$$

The problem is transient due to the time dependent domain occupied by the material and the energy equations (5.1.3) and (5.1.7). Further, it is non-linear, mainly because of the complex dependence of the viscosity upon temperature and shear rate. The problem is three-dimensional with respect to the continuity and the energy equation. The pressure, however, is independent of the z coordinate. The flow front is assumed to be flat in the z direction and, consequently, the position is not a function of the z coordinate.

Analogous to Hieber and Shen (1980), a finite element/finite difference method is applied in which the quantities with respect to the coordinates of the midplane are discretized in terms of finite elements, while a finite difference procedure is chosen to describe the variations in the z direction and in time. This formulation is particularly suitable for handling cavities with very complex three-dimensional forms.

For general literature about the finite element and the finite difference techniques see: Bathe and Wilson (1976); Ziekiewicz (1977); Lapidus and Pinder (1982).

The finite element mesh is spatially fixed (Eulerian description) and covers the whole midplane of the cavity. The finite difference grid in z direction is fitted at every vertex covering the fluid and the two solidified layers against the cooled walls. In the fluid a Gaussian grid point distribution will be chosen, with the advantage that integrals over the entire fluid phase can be evaluated accurately. Further, the point density increases towards the solidified layers where considerable gradients appear.

In Fig. 5.1.1, a finite element is sketched with the finite difference grids fitted at the vertices. In order to visualize the grid point distributions properly the figure is elongated in the z direction.

The problem is solved in a number of time steps. After each time step, the new position of the flow front is calculated. On the sides of the elements which are intersected by the flow front temporary nodes will be created and the covered part of the intersected elements divided into one or more sub-elements, in such a manner that a proper mesh is obtained for the whole actual domain.
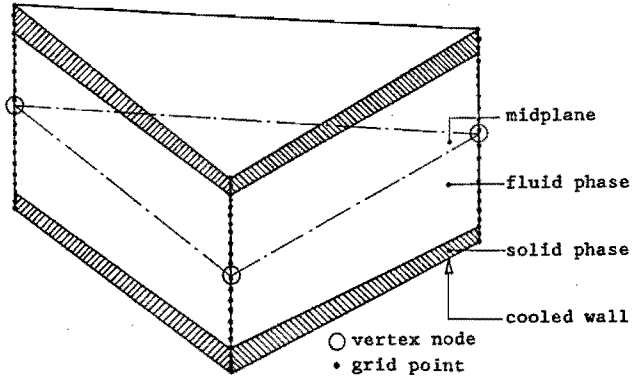
Fig. 5.1.1 Grid point distributions at the vertices of a finite element.

An iteration process will be started in which all the relevant equations are solved successively. As a first estimation of the important quantities, the values calculated for the previous point of time will be chosen. For the values of the quantities in the grid points of the nodes which just have entered the fluid, an appropriate estimation will be made.

The iteration process globally is composed of the steps given below.

1) Solution of an adapted form of the momentum equation in the fluid phase, this will result in a new estimation for the pressure p and the velocity $\vec{v}^*$ (Paragraph 5.3). Subsequently the viscosity η and the mass density ρ are updated.

2) Solution of the continuity equation in the solid and the liquid domains. This will result in a new estimate of the velocity component v_z (Paragraph 5.4).

3) Updating of the thermal conductivity λ and thermal capacity c_p. Solution of the energy equations in both the solid and liquid phases, in order to get the new temperature distribution (Paragraph 5.5).

4) Calculation of the new positions of the solid-liquid interfaces using the jump relation with respect to energy (5.1.10) (Paragraph 5.6).

5) Convergence check with respect to pressure, temperature and posi-
   tions of the solidified layers. If necessary, the steps 1 until 5
   will be repeated.

After convergence, a new time step will be made and the whole process
repeated.

5.2   Propagation of the flow front

The midplane of the cavity is divided into spatially fixed finite
elements. The flow front moves through the mesh. At the intersected
element edges, temporary nodes are created. Connection of the ad-
jacent temporary nodes by straight lines, delivers the new approxima-
tion of the flow front. The sections of the partly filled elements
which are in the fluid will be divided into three node sub-elements.
Fig. 5.2.1 shows some examples of the sub-divisions for meshes with
three and six node triangles and four and eight node quadrilaterals.

■ temporary nodes
O ● fixed nodes
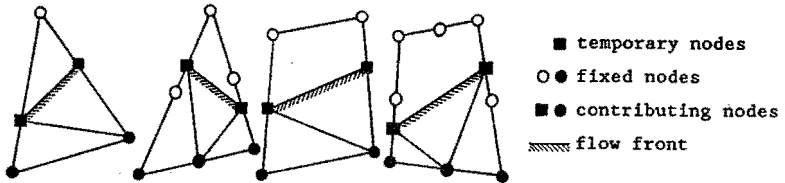■ ● contributing nodes
〜〜〜 flow front

Fig. 5.2.1 sub-divisions into three node elements.

Considering the fixed mesh, only the nodes in the fluid contribute to
the finite element formulation. Fig. 5.2.2 shows that an element may
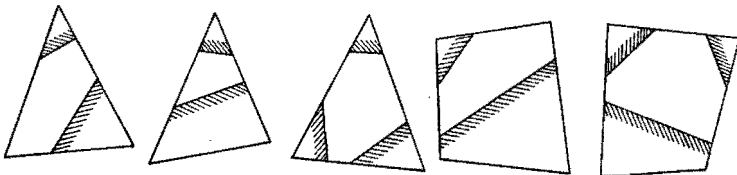be intersected by more than one flow front.

Fig. 5.2.2 Elements with several flow fronts.

The complete flow front consists of a number of connected edges of sub-elements. The velocity of the flow front is made equal to the average velocity $\vec{v}_a^*$ in the connected sub-element. This velocity is perpendicular to the flow front (Paragraph 5.3).

During a time increment Δt the displacement $\vec{\Delta x}^*$ of each line segment of the flow front will be determined, using an explicit Euler integration scheme

$$\vec{\Delta x}^* = \int_{t-\Delta t}^{t} \vec{v}_a^* dt = \vec{v}_a^*(t - \Delta t)\Delta t \qquad (5.2.1)$$

Applying (5.2.1) at every line segment separately, leads to results which are unsuitable for use, because the new flow front will be discontinuous, due to discretization errors. Moreover, if the midplane is curved, it will not coincide with the plane.

For plane geometries with convex contours, the method proposed by Bonnerot and Jamet (1977) can be applied successfully, in order to get a continuous flow front. In general however, different techniques are required. Therefore, the following method has been developed.

Every point of the segmented flow front can be regarded as a source, covering an area on the midplane. The boundary of this area will have such a form, the shortest distance from each point of the boundary to the source, measured along the midplane, will equal $|\vec{\Delta x}^*|$. The intersections of the total envelope of all these boundaries with the element edges will supply the new temporary nodes, then, the new flow front can be constructed.
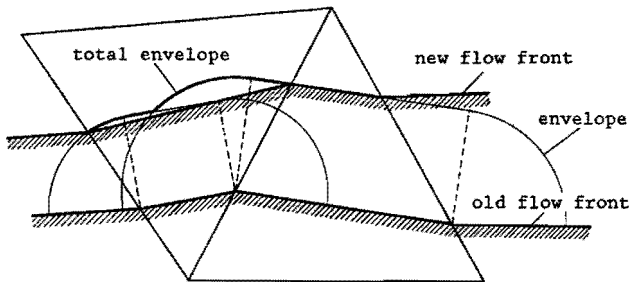

Fig. 5.2.3 Construction of the flow front.

Fig. 5.2.3, shows the construction of a flow front in two elements in the case, the midplane is not curved (the boundary of the area covered by a source reduces to a circle then). An advantage of this method is that geometries with a concave contour can be dealt with easily. Also, dividing the flow front by a partition of the cavity causes no problems at all (Fig. 5.2.4).
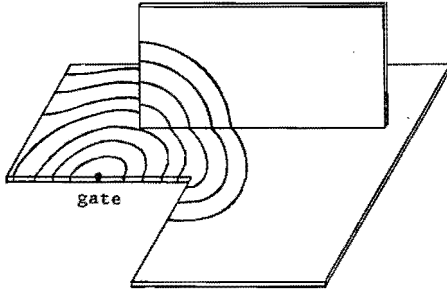

Fig. 5.2.4 Flow fronts in a complex geometry.

It has to be noted that the method above, based on an explicit Euler scheme, for all the numerical simulations carried out produced a flow front without the development of oscillations. Therefore, contrairy to the results of Hieber and Shen (1980), no predictor corrector method has to be used to obtain stability.
It is quite clear that the conservation of mass is violated by this procedure. Therefore, a general correction will be carried out. For that purpose several methods can be used. It would have been possible to determine the new position of the flow front iteratively, keeping the time steps constant. However, the simpler method is chosen for, adapting the time steps, in such a way that, combined with the predicted flow fronts, global conservation of mass is satisfied. Mostly, the initial value of the time step is chosen in such a way that, the distance between two successive flow fronts does not exceed a certain predefined value.

5.3 Momentum equation

In this Paragraph, a method is presented for determining the pressure distribution p and the velocity distribution $\vec{v}^*$ of the fluid in the filled part of the mould. For this purpose, with respect to the midplane, a semi two-dimensional pressure problem can be formulated. If the pressure distribution is known the velocity $\vec{v}^*$ as a function of the z coordinate can be calculated, with an integration procedure in the z direction.

Integration of the momentum equation with respect to the z direction
Since the pressure does not depend on the z coordinate, the first relation of (5.1.2) can be integrated with respect to this coordinate in order to produce

$$\frac{\partial \vec{v}^*}{\partial z} = \frac{z}{\eta}\vec{\nabla}^* p + \frac{\vec{C}}{\eta} \tag{5.3.1}$$

where $\vec{C}$ is a yet undetermined vector, that does not depend on z. The domain of the fluid phase in the z direction is bounded by the two solidified layers, $\alpha^- \leq z \leq \alpha^+$. The velocity $\vec{v}^*$ as a function of z can be found by integrating (5.3.1) from α^- to z, yielding

$$\vec{v}^* = \int_{\alpha^-}^{z} \frac{\partial \vec{v}^*}{\partial z} dz = (\int_{\alpha^-}^{z} \frac{z}{\eta} dz) \vec{\nabla}^* p + (\int_{\alpha^-}^{z_1} \frac{1}{\eta} dz) \vec{C} \tag{5.3.2}$$

where, it is used, that on the solid-liquid interface $z = \alpha^-$, holds $\vec{v}^* = \vec{0}$. For $z = \alpha^+$, $\vec{v}^*$ is also zero. Using this boundary condition, for $\vec{C}$ can be derived

$$\vec{C} = - (\int_{\alpha^-}^{\alpha^+} \frac{z}{\eta} dz) \vec{\nabla}^* p / \int_{\alpha^-}^{\alpha^+} \frac{1}{\eta} dz \tag{5.3.3}$$

The integrals in the relation above appear frequently. Therefore, the following brief notations are introduced

$$J_0 = \int_{\alpha^-}^{\alpha^+} \frac{1}{\eta} dz \quad ; \quad J_1 = \int_{\alpha^-}^{\alpha^+} \frac{z}{\eta} dz \tag{5.3.4}$$

From these definitions, the vector $\vec{C}$ can be written as

$$\vec{C} = - \frac{J_1}{J_0} \vec{\nabla}^* p \tag{5.3.5}$$

and substituting it in (5.3.2) gives

$$\vec{v}^* = (\int_{\alpha^-}^{z} \frac{1}{\eta}(z - \frac{J_1}{J_0}) dz) \vec{\nabla}^* p \tag{5.3.6}$$

If an estimation of the pressure and viscosity distributions, as well as, the positions of the solidified layers are known, relation (5.3.6) can be used to calculate the velocity parallel to the mid-plane. Integrating $\vec{v}^*$ over the entire channel height delivers the following relation that will be used later

$$\int_{\alpha^-}^{\alpha^+} \vec{v}^* dz = - S \vec{\nabla}^* p \tag{5.3.7}$$

where

$$S = J_2 - \frac{J_1}{J_0} J_1 \quad ; \quad J_2 = \int_{\alpha^-}^{\alpha^+} \frac{z^2}{\eta} dz \tag{5.3.8}$$

If the problem is symmetrical with respect to the midplane, easily can be proved that $J_1 = 0$. In that case the relations (5.3.6) and (5.3.8) can be simplified.

Formulation of the pressure problem

In order to obtain an approximation for the pressure, as a starting point, the weighted residuals formulation of the continuity equation (5.1.1) is chosen

$$\int_V w(\vec{\nabla}^*\cdot\vec{v}^* + \frac{\partial v_z}{\partial z} + \frac{\dot{\rho}}{\rho})dV = 0 \tag{5.3.9}$$

with V the liquid polymer volume injected into the mould. Requiring (5.3.9) to hold for every (piecewise continuous) function w, is equivalent with the requirement that (5.1.1) is satisfied.
The weighting function w is taken to be independent of the z coordinate.
Since a flat flow front in z direction is assumed, the integral over the volume V can be decomposed into a surface integral with respect to the covered area A of the midplane and a line integral from $z = \alpha^-$ to $z = \alpha^+$. Since $\vec{\nabla}^*$ and w are independent of z and $\vec{v}^* = 0$ for $z = \alpha^-$ and $z = \alpha^+$, (5.3.9) transforms into

$$\int_A w\vec{\nabla}^*\cdot(\int_{\alpha^-}^{\alpha^+}\vec{v}^*dz)dA + \int_A w(\int_{\alpha^-}^{\alpha^+}\frac{\partial v_z}{\partial z}dz)dA +$$

$$+ \int_A w(\int_{\alpha^-}^{\alpha^+}\frac{\dot{\rho}}{\rho}dz)dA = 0 \tag{5.3.10}$$

Using relation (5.3.7), it can be seen that

$$\int_A w\vec{\nabla}^*\cdot(S\vec{\nabla}^*p)dA = \int_A w[v_z(\alpha^+) - v_z(\alpha^-)]dA + \int_A w(\int_{\alpha^-}^{\alpha^+}\frac{\dot{\rho}}{\rho}dz)dA \tag{5.3.11}$$

Integration by parts of (5.3.11), with the theorem of Gauss, leads to a weak form suitable for discretization with piecewise differentiable fields for p

$$\int_A S\vec{\nabla}^*w\cdot\vec{\nabla}^*p\,dA = \int_B wS\vec{\nabla}^*p\cdot\vec{n}dB - \int_A w[v_z(\alpha^+) - v_z(\alpha^-)]dA +$$

$$- \int_A w(\int_{\alpha^-}^{\alpha^+}\frac{\dot{\rho}}{\rho}dz)dA \tag{5.3.12}$$

where B is the boundary of the surface A and $\vec{n}$ the unit outward
normal at A. Along the full boundary length (the distinct parts are
indicated in Fig. 5.3.1), the boundary conditions have to be pre-
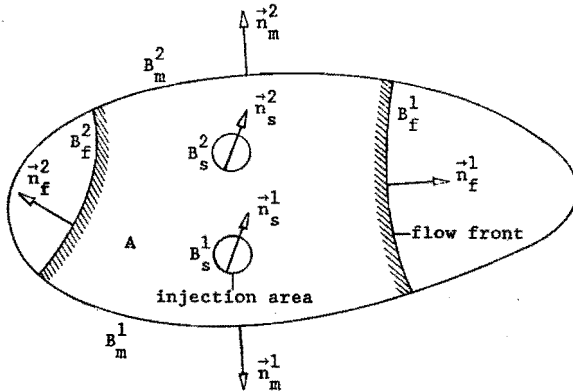scribed. These conditions are of the Dirichlet or Neumann type.

Fig. 5.3.1 Boundary of surface A.

The polymer is injected through the edges B_s^i, the parts of the bound-
ary B_f^j represent the flow front and the parts B_m^k are in contact with
the mould.

At the flow front the pressure, is assumed to be negligible

$$p = 0 \qquad \text{on } B_f^i \ (i = 1, 2, ..) \tag{5.3.13}$$

No fluid can penetrate through the wall of the mould, thus, $\vec{v}^* \cdot \vec{n}_m^k = 0$.
Therefore, with relation (5.3.6) follows

$$\vec{\nabla}^* p \cdot \vec{n}_m^k = 0 \qquad \text{on } B_m^k \ (k = 1, 2, ..) \tag{5.3.14}$$

With the introduction of the boundary flux (per unit of length)

$$q = S \vec{\nabla}^* p \cdot \vec{n} \tag{5.3.15}$$

from (5.3.12), can be derived that

$$\int_A S\vec{\nabla}^*w \cdot \vec{\nabla}^*p\,dA = \sum_i \int_{B_s^i} wq_s^i dB + \sum_j \int_{B_f^j} wq_f^j dB +$$

$$- \int_A w[v_z(\alpha^+) - v_z(\alpha^-)]\,dA - \int_A w(\int_{\alpha^-}^{\alpha^+} \frac{\dot{\rho}}{\rho}\,dz)\,dA \qquad (5.3.16)$$

Relation (5.3.16) is non-linear with respect to p, because several of the quantities appearing in this equation are non-linear functions of p. The pressure p will be solved iteratively, using a Picard scheme, where S and the righthand side are evaluated from the results of the previous iteration cycle.

Discretization

Equation (5.3.16) will be elaborated by the finite element method, in order to determine an approximation for p. On the surface A the pressure field will be discretized, therefore A is divided into elements (including the sub-divisions of the elements intersected by the flow front). The total number of nodes in A, where the pressure has to be evaluated, is equal to N. The column of nodal pressures is indicated by

$$p_n \ (n = 1,2,\ldots,N) \qquad \text{or} \qquad \underset{\sim}{p} \qquad (5.3.17)$$

The pressure at all the other points of A can be obtained by inter-polation according to

$$p = \sum_{n=1}^{N} \phi_n p_n \qquad \text{or} \qquad p = \underset{\sim}{\phi}^T \underset{\sim}{p} \qquad (5.3.18)$$

where the interpolation functions ϕ_n obey the usual requirements. From now on, the short notation with the tilde in order to indicate a column will be used.

For the gradient of the pressure $\vec{\nabla}^*p$ it follows that

$$\vec{\nabla}^*p = \vec{\nabla}^*\underset{\sim}{\phi}^T \underset{\sim}{p} \qquad (5.3.19)$$

According to the method of Galerkin the weighting function w is discretized in the same manner as the pressure

$$w = \underset{\sim}{\phi}^T \underset{\sim}{w} = \underset{\sim}{w}^T \underset{\sim}{\phi} \qquad (5.3.20)$$

Substituting of (5.3.18), (5.3.19) and (5.3.20) the weighted residuals equation (5.3.16) becomes

$$\underset{\sim}{w}^T (\int_A S \vec{\nabla}^* \underset{\sim}{\phi} \cdot \vec{\nabla}^* \underset{\sim}{\phi}^T dA) \underset{\sim}{p} = \underset{\sim}{w}^T (\sum_i \int_{B_s^i} \underset{\sim}{\phi} q_s^i dB + \sum_j \int_{B_f^j} \underset{\sim}{\phi} q_f^j dB) +$$

$$- \underset{\sim}{w}^T \int_A \underset{\sim}{\phi} [v_z(\alpha^+) - v_z(\alpha^-)] dA - \underset{\sim}{w}^T \int_A \underset{\sim}{\phi} (\int_{\alpha^-}^{\alpha^+} \frac{\dot{\ell}}{\rho} dz) dA \qquad (5.3.21)$$

The injection areas will be modelled with a number of point sources located at the nodes. A film injection is replaced by a number of adjoining point sources. The sum of the integrals over the injection boundaries B_s^i in (5.3.21) can be replaced by a column $\underset{\sim}{Q}$, where the associated injected volume fluxes are substituted, at the places corresponding to the positions of the "injection" nodes. All the other values of that column are zero.

Requiring that (5.3.21) is satisfied for every admissible column $\underset{\sim}{w}$ results in

$$\underline{K} \underline{p} = \underset{\sim}{Q} + \underset{\sim}{R} - \underset{\sim}{V} - \underset{\sim}{U} \qquad (5.3.22)$$

where

$$\underline{K} = \int_A S \vec{\nabla}^* \underset{\sim}{\phi} \cdot \vec{\nabla}^* \underset{\sim}{\phi}^T dA \qquad (5.3.23)$$

$$\underset{\sim}{R} = \sum_j \int_{B_f^j} \underset{\sim}{\phi} q_f^j dB \qquad (5.3.24)$$

$$\underset{\sim}{V} = \int_A \underset{\sim}{\phi} [v_z(\alpha^+) - v_z(\alpha^-)] dA \qquad (5.3.25)$$

$$\underset{\sim}{U} = \int\limits_{A} \phi (\int\limits_{\alpha^-}^{\alpha^+} \frac{\dot{\rho}}{\rho} dz) dA \qquad (5.3.26)$$

How, the quantities v_z and $\dot{\rho}/\rho$ are obtained will be discussed later. The column $\underset{\sim}{p}$ contains a number of zeros, related to the nodes at the flow front, see (5.3.13). The corresponding components of $\underset{\sim}{R}$, however, have an unknown value at these positions, while the rest of the column $\underset{\sim}{R}$ is empty. This knowledge can be used for partitioning (5.3.22), which results in a standard symmetrical linear system of equations, where, the column $\underset{\sim}{R}$ is not incorporated anymore. Using an ordinary procedure for the solution (Bathe and Wilson, 1976) a new estimation for the pressure distribution can be calculated.

Calculation of the velocity $\vec{v}^*$, the viscosity η and the density ρ

From (5.3.6), it is clear that the velocity $\vec{v}^*$ and the pressure gradient $\vec{\nabla}^* p$ have the same direction. The vector $\vec{\nabla}^* p$ is independent of z and can be evaluated in the elements. The magnitude $|\vec{v}^*|$ of the velocity will be calculated on the grid lines connected to the vertices of the elements with

$$|\vec{v}^*| = | \int\limits_{\alpha^-}^{z_1} \frac{1}{\eta} (z - \frac{J_1}{J_0}) dz | | \vec{\nabla}^* p | \qquad (5.3.27)$$

The shear rate $\dot{\gamma}$ can be derived from $\vec{v}^*$ using (5.1.4), (5.3.1) and (5.3.5) it follows

$$\dot{\gamma} = | \frac{1}{\eta} (z - \frac{J_1}{J_0}) | | \vec{\nabla}^* p | \qquad (5.3.28)$$

As mentioned $|\vec{\nabla}^* p|$ can be evaluated in every element. In general it will not be continuous across the element boundaries. For a particular node, $|\vec{\nabla}^* p|$ will be calculated, from the information of the elements containing that node, evaluating $|\vec{\nabla}^* p|$ at the centroid of each element and averaging the weighted contribution of the elements. The choice of a weighting factor is rather arbitrary (for example the

weighting factor may be proportional to the angle subtended at the particular node, inversely proportional to the distance from the given node to the centroid of the element, etc).

The term $(z - J_1/J_0)/\eta$ which appears in (5.3.27) and (5.3.28) will be evaluated from the results of the previous iteration cycle.

With the new values of the pressure and the shear rate, the density ρ = $\rho(p,T)$ in the solid and the fluid domain, as well as, the viscosity $\eta = \eta(\dot{\gamma},T,p)$ in the fluid phase can be updated, the temperature values from the previous iteration cycle being used.

Finally, new values for the integrals J_0, J_1 and J_2 according to (5.3.4) and (5.3.8) are determined.

5.4   Continuity equation

In this Paragraph, the continuity equations for the fluid and the solidified layers will be solved, offering a new estimation for the velocity component v_z at every grid point.

For the positions α^+ and α^- of the solid-liquid interface, the values of the previous iteration cycle will be taken and the updated values will be used, for ρ and $|\vec{v}^*|$.

Solid phase
In the solidified layers, distributions with equidistant grid points are defined on every grid line in such a manner that the distance between two adjacent points does not exceed a predefined value. Consequently, the number of grid points will increase when the solidified layers grow.

Using the definition of the material time derivative the continuity equation according to (5.1.5) can be transformed to

$$\rho\frac{\partial v_z}{\partial z} + \frac{\partial \rho}{\partial z}v_z = -\frac{\partial \rho}{\partial t} \tag{5.4.1}$$

Where $\partial\rho/\partial t$ is the spatial time derivative of ρ. This equation will be solved numerically, using a stable backwards difference scheme, of which several computational molecules are displayed in Fig. 5.4.1, for the solidified layer with $-\frac{h}{2} \leq z \leq \alpha^-$ (Lapidus and Pinder, 1982).
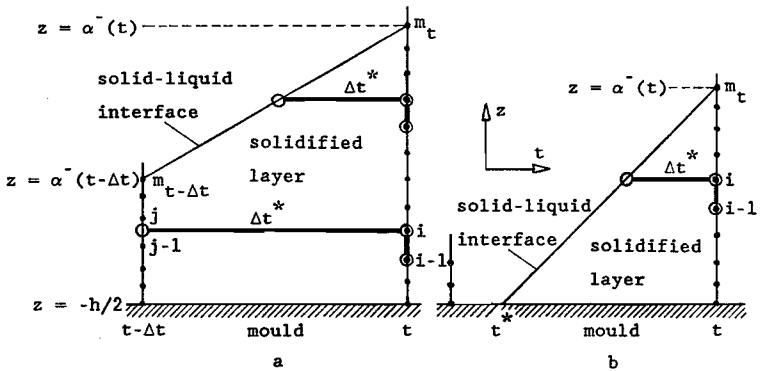
Fig. 5.4.1 Computational molecules in the solidified layer.

The spatial time derivative of ρ will be approximated by a backwards difference scheme. The difference between the value of ρ at a grid point i for the present time t and ρ at the same spatial location for time $t-\Delta t^*$ has to be determined. The time interval Δt^* is equal to or less than the time step Δt (Fig. 5.4.1). The value ρ for time $t-\Delta t^*$, in the case $\Delta t^* = \Delta t$, can be found by interpolating between the values in the gridpoints j-1 and j. If a solidified layer is inserted, the interpolation between the values at the grid points $m_{t-\Delta t}$ and m_t can be made (the velocity of the solid-liquid interface is assumed constant during Δt).

If, at time $t-\Delta t$, the fluid has not reached the grid line, this procedure need to be adapted. At time t^*, the grid line enters the fluid, it will be assumed that the thickness of the solidified layer is equal to zero (Fig. 5.4.1b). The value of ρ at time $t-\Delta t^*$ can be found by interpolating at the solid-liquid interface.

The derivatives with respect to z will be approximated from the values of the related quantities at the grid points i-1 and i. With the condition that v_z equals zero at the wall, $z = -h/2$, the discretized equation (5.4.1) can be solved for $i = 2,3,..,m_t$, successively, resulting in a new estimate for the velocity v_z.

For the solidified layer for $z = \alpha^+$ the calculations can be performed analogously.

solid-liquid interface

In order to determine the values of $v_z^f(\alpha^-)$ and $v_z^f(\alpha^+)$ as boundary
conditions for the continuity equation in the fluid phase, the jump
relation according to (5.1.8) has to be solved for both the solid-
liquid interfaces. For the quantities ρ^s, ρ^f and v_z^s the during the
iteration cycle, updated values will be chosen, where v_z^s is the
solution of (5.4.1) at the grid point on the interface. The velocity
component u_z of the solid-liquid interface is calculated in the
previous iteration cycle. In order to specify the jump in certain
quantities on the solid-liquid interface, two coinciding grid points
are defined, both in the fluid and the liquid.

Fluid phase

In the fluid phase, a Gaussian grid point distribution is defined,
with the same number of points and two extra points at the solid-
liquid interfaces, on every grid line.
The continuity equation for the fluid according to (5.1.1), with the
material time derivative $\dot{\rho}$ as an addition of the spatial time deriva-
tive and the convective part, reads

$$\frac{\partial v_z}{\partial z} = -\frac{v_z}{\rho}\frac{\partial \rho}{\partial z} - \frac{1}{\rho}\left(\frac{\partial \rho}{\partial t} + \vec{v}^*\cdot\vec{\nabla}^*\rho\right) - \vec{\nabla}^*\cdot\vec{v}^* \tag{5.4.2}$$
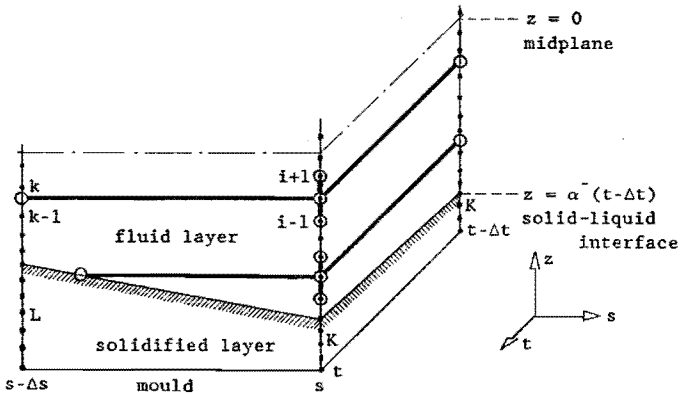

Fig. 5.4.2 Computational molecules in the fluid layer.

This equation will be solved using a stable backwards implicit finite difference scheme, of which two possible computational molecules are displayed in Fig. 5.4.2.

The spatial time derivative of ρ will be approximated in the same manner as for the solidified layers.

For the grid lines that have entered the fluid during this time step, an estimation of ρ as a function of z, at the entrance time t^* has to be made. In Appendix 4 it is explained, how this goal can be achieved with a simple fountain flow model.

The derivatives with respect to z will be approximated with a central difference scheme, using the values of the related quantities at the grid points i-1, i and i+1.

The terms $\vec{V}^* \cdot \vec{V}\rho$ and $\vec{V}^* \cdot \vec{v}$ will be evaluated in the direction of the flow, based on a backwards difference scheme, using the interpolated values between the grid points k-1 and k on grid line L which is situated up-stream at a distance Δs from the grid line K. In order to find the position of the grid line L, starting from grid line K, the up-stream flow path through one of the connected elements will be constructed, using the direction of the flow in that specific element (Fig. 5.4.3a). Grid line L will be defined at the intersection of the flow path with the opposite element edge. The values of the desired quantities at the grid points of the line L can be found by linearly interpolating between the values of the corresponding grid points of the grid lines M and N.
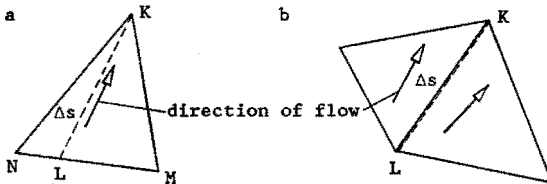

Fig. 5.4.3 The up-stream flow paths.

In Fig. 5.4.3b, is indicated that in several cases a flow path along an element edge can be assumed reasonable.

Usually, only one up-stream flow path will be found. In cases where
there are two or more possible flow paths, the relevant values will
be calculated at all the grid points, for every flow path, and these
values will be averaged afterwards.

The discretized form of equation (5.4.2) is of the first order,
however, it has two boundary conditions at the solid-liquid inter-
faces. In order to satisfy both of these conditions, a least square
method is applied. This method produces a linear tridiagonal system
of equations which can be solved with a standard technique (Lapidus
and Pinder, 1982) providing a new approximation of v_z in the fluid
domain.

5.5   Energy equation

In this Paragraph, the solution of the energy equation in the fluid,
as well as in the solid layers, will be discussed. For the positions
α^+ and α^- of the solid-liquid interfaces, the values of the previous
iteration cycle will be chosen. For λ and c_p, new values will be
calculated using the updated ρ and the temperatures from the previous
iteration cycle.

Approximation in solid and fluid domain

The energy equations in both the fluid and solid domains are given in
(5.1.3) and (5.1.7), respectively. Apart from the viscous dissipation
term $\eta\dot{\gamma}^2$, these equations are identical.

The material time derivative of the temperature can be decomposed
into a spatial and a convective part according to

$$\dot{T} = \frac{\partial T}{\partial t} + v_z\frac{\partial T}{\partial z} + \vec{v}^*\cdot\vec{\nabla}^* T \qquad (5.5.1)$$

In the solid phase, the last term of (5.5.1) will disappear. The
spatial time derivative $\partial T/\partial t$ will be handled in the same manner as
$\partial \rho/\partial t$ in the previous Paragraph, including an estimate of the tem-
perature distribution according to Appendix 4, for the grid lines
that enter the fluid during this step. The derivative $\partial T/\partial z$ will be
discretized implicitly by a central difference scheme. The most

crucial point appears to be the evaluation of the convective term
$\vec{v} \cdot \vec{\nabla}^* T$. Numerical experiments have shown that, in order to obtain any
stable solution, this term has to be approximated with a backwards
difference scheme (Hieber and Shen (1980) also mentioned this). The
numerical scheme can be applied successfully, with the computational
molecules as discussed in Paragraph 5.4.

The conduction term of the energy equation can be written as

$$\frac{\partial}{\partial z}(\lambda \frac{\partial T}{\partial z}) = \frac{\partial \lambda}{\partial z} \frac{\partial T}{\partial z} + \lambda \frac{\partial^2 T}{\partial z^2} \qquad (5.5.2)$$

Also, in this case, the derivatives that appear will be approximated
implicitly with a central difference scheme.

The viscous dissipation term, which occurs only in the fluid, will be
evaluated implicitly too.

The last term in the energy equation reads $T(\partial \rho/\partial T)_p \dot{p}/\rho$ with

$$\dot{p} = \frac{\partial p}{\partial t} + \vec{v} \cdot \vec{\nabla}^* p \qquad (5.5.3)$$

where, p is not a function of the z coordinate. The approximation of
$\dot{p}$ will be performed in the way described above. The term $(\partial \rho/\partial T)_p$ is
a material property which can be evaluated simply.

for every grid line in the liquid, as well as the solid phases, three
tridiagonal matrix equations can be derived. With the prescribed wall
temperatures and the estimated solidification temperatures, these
matrix equations can be solved, producing a new temperature distribu-
tion.

5.6   Positions of the solid-liquid interfaces

The positions of the solid-liquid interfaces will be calculated
directly from the jump relation with respect to energy (5.1.10). The
velocity component u_z of the solid-liquid interfaces can be approxi-
mated by a backwards difference scheme. For the solid-liquid inter-
face belonging to $z = \alpha^-$ it follows that

$$u_z = \frac{\alpha^-(t) - \alpha^-(t - \Delta t)}{\Delta t} \tag{5.6.1}$$

Substituting (5.6.1) in (5.1.10) leads to

$$\frac{\alpha^-(t) - \alpha^-(t - \Delta t)}{\Delta t} - F(\alpha^-(t)) = 0 \tag{5.6.2}$$

where, $F(\alpha^-(t))$ is used as an abbreviation for

$$F(\alpha^-(t)) = v_z^s + \frac{1}{(\Gamma + \frac{\rho^s - \rho^f}{\rho^s \rho^f} p)\rho^s}[\lambda^s(\frac{\partial T}{\partial z})^s - \lambda^f(\frac{\partial T}{\partial z})^f] \tag{5.6.3}$$

Solution of $\alpha^-(t)$ from (5.6.2) is difficult, because a small change in $\alpha^-(t)$ affects this function tremendously. Numerical calculations have shown that the function $F(\alpha^-(t))$ has the profile as shown in Fig. 5.6.1.
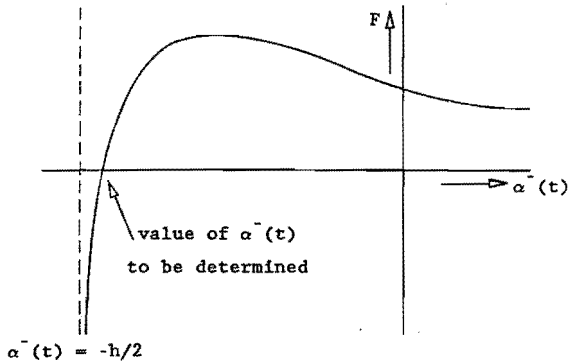

Fig. 5.6.1 Curve of the function F.

The character of the curve invites to choose for a bisection method for the solution of $\alpha^-(t)$. The convergence rate appears satisfactory. For all the quantities in (5.6.3), the during this iteration cycle updated values are taken. The derivatives with respect to z are evaluated with three point approximations.

The position of the solid-liquid interface for $z = \alpha^+$ is calculated analogously.

5.7   Recapitulation

The essential part of the numerical process, generally seen, has been
presented in the next flow diagram. This diagram contains all the
steps discussed earlier in this Chapter. A brief description of the
steps, which are indicated by the numbers in the diagram, is in-
cluded.
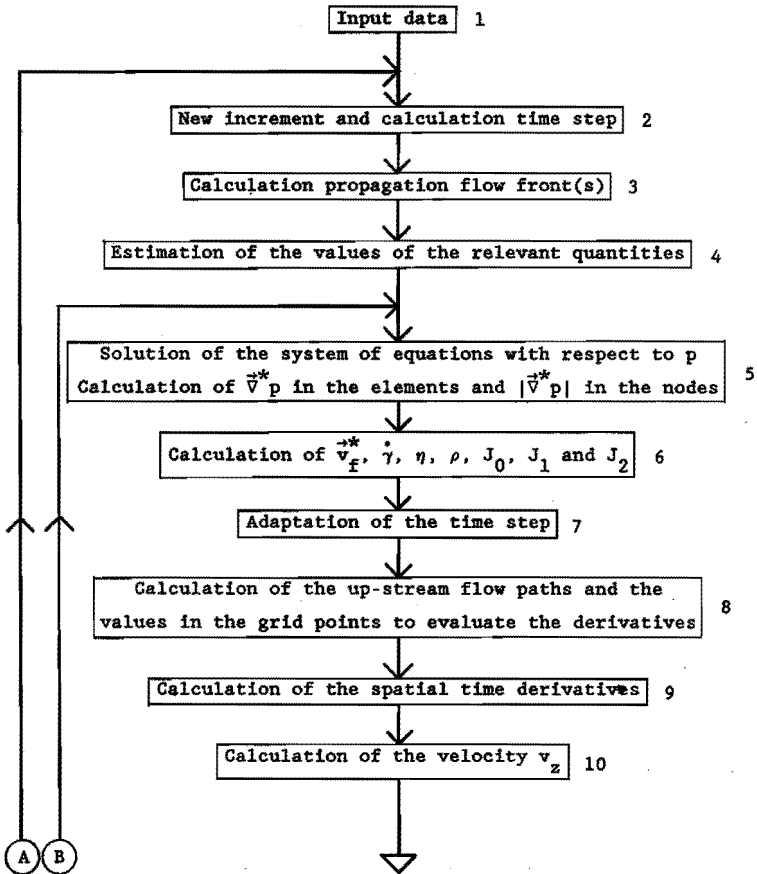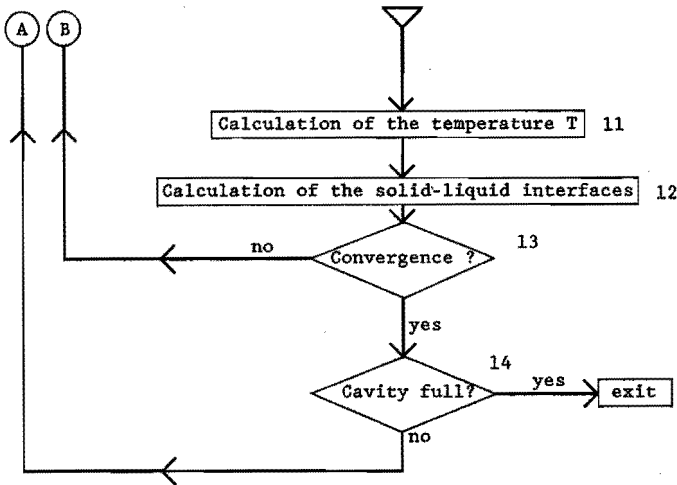
1) Input of geometric data, the process parameters and material properties.

2) Two alternatives are available. Either the maximum distance the flow front advances is chosen, or the time increment. In the first case, the time increment will be calculated from the maximum velocity at the flow front and the prescribed propagation of the flow front.

3) Calculation of the propagation of the flow front as discussed in Paragraph 5.2.

4) At the start of the iteration process, first estimations of the values of the important quantities are needed. For grid lines in the fluid for more than one time step, the values of the previous time will be taken. When the grid line has just entered the fluid, the values at the previous time of a grid line, situated up-stream, will be copied.

5) The system of equations is formed by assembling the contributions of the individual elements. The system is solved in order to get a new approximation for the pressure field. Calculation of $\vec{\nabla}^* p$ in the centroid of each element, as well as, $|\vec{\nabla}^* p|$ in the nodes by a weighted average over the connected elements, see Paragraph 5.3.

6) Calculation of the velocity $\vec{v}_f^*$ in the direction of the flow and the shear rate $\dot{\gamma}$, at all the grid points in the fluid. Updating of the viscosity η and the mass density ρ. Further, new evaluations of the integrals J_0, J_1 and J_2 will be made for every grid line in the fluid.

7) The total mass in the cavity will be calculated from the included volume and the approximated mass density of the polymer. Knowing the total mass in the cavity at the previous time, allows an adjustment of the time step to be determined, using the pre- scribed volume fluxes and the approximated mass densities at the injection points.

8) In order to evaluate the derivatives in the direction of the flow: $\vec{\nabla}^* \rho$, $\vec{\nabla}^* \cdot \vec{v}^*$, $\vec{\nabla}^* T$ and $\vec{\nabla}^* p$, the up-stream flow paths starting from every mode will be calculated. If an element edge is inter- sected a provisional grid line is created. All the values of the important quantities at every grid point are calculated by linear interpolation between the values at the corresponding grid points of the grid lines at the end of the relevant edge (Paragraph 5.4).

9) Calculation of the spatial time derivatives $\partial \rho / \partial t$ and $\partial T / \partial t$ at all the grid points, using the approximated value of the time step and the values of ρ and T at the previous time (Paragraph 5.4). If a grid line was not in the fluid at the previous time, an approximation of the mass density and the temperature will be made at the time that the grid line enters the fluid (Appendix 4). The maximum time interval then equals the time when the grid line enters the fluid subtracted from the present time.

10) Solution of the continuity equation, for the solid layer, at the solid-liquid interface and for the fluid layer, resulting in a new approximation for the velocity component v_z (Paragraph 5.4).

11) Solution of the energy equations for the solid and liquid layers, producing a new approximation of the temperature distribution (Paragraph 5.5).

12) Calculation of the new position for the solid-liquid interfaces on all the grid lines (Paragraph 5.6).

13) Convergence check with respect to the pressure, position of the
    solidified layers and temperature in the core of the flow.

14) when the cavity is not filled yet a new increment will be made.

Numerical experiments have shown that the velocity component v_z
cannot be evaluated accurately enough. The inaccuracy of v_z probably
can be explained from the poor approximation of $\vec{\nabla}^*\cdot\vec{v}^*$ in (5.4.2)
which, according to (5.3.6), is proportional to $\vec{\nabla}^*\cdot\vec{\nabla}^* p$. The discre-
tization chosen for p is unsuitable for delivering a reliable estima-
tion for this term. Applying a higher order element (parabolic in-
stead of linear) will not reduce the problem, because $\vec{\nabla}^* p$ remains
discontinuous across the element sides. This leads to the suggestion
that an element has to be formulated, with at least $\vec{\nabla}^* p$ continuity
across the element edges.

6   NUMERICAL SIMULATIONS

6.1   Introduction

In this Chapter, the results of numerical simulations are presented
and evaluated. In Paragraph 6.2, the flow fronts predicted will be
compared with the experimental results, by injecting a Newtonian
fluid between two parallel plates under isothermal conditions.
The Paragraphs 6.3 - 6.5 give the results of numerical simulations
for the injection of non-Newtonian fluids under non-isothermal condi-
tions.
In Paragraph 6.3, attention is focussed on the injection of a centre
gated disk, in order to investigate the influence of various material
parameters. Also, the accuracy in approximating the temperature
distribution is evaluated for low injection velocities.
In Paragraph 6.4, the filling of a rectangular mould is calculated.
The results are compared with experimental and numerical data from
literature.
Finally, the injection into a three-dimensional cavity with sudden
varying heights is simulated. The predicted flow fronts are compared
to short shots made into an experimental mould with the same dimen-
sions.
It should be noted that in all the simulations carried out, the
velocity component v_z in the direction of the channel height was not
taken into account, because this velocity component cannot be deter-
mined accurately enough, as mentioned at the end of Chapter 5.

6.2   Verification of the flow front propagation, for an isothermal
       Newtonian flow in a complex flat geometry

In order to evaluate the numerical method for calculating a new
location of the flow front (Paragraph 5.2), some simple experimental
simulations with a model fluid were carried out. Basically, the
experimental set-up consists of two parallel transparant flat plates,
between which a fluid with a Newtonian behaviour can be injected. The
desired contour of the cavity is composed of interchangeable strips

between the two plates. The fluid is injected at a constant rate into
the cavity, through one or more holes in one of the plates. For the
experiments, glycerol was used which had a viscosity of 1.13 Pas. The
cavity was kept horizontal, in order to reduce to a minimum the
influence of gravity on the fluid. The fluid was injected at such a
low speed that inertial forces could be neglected with respect to the
viscous forces. The propagation of the flow front during the injec-
tion process was recorded on a video tape.
The cavity in Fig. 6.2.1 is chosen for investigating flow around
sharp corners and division of flow. The channel height of the cavity
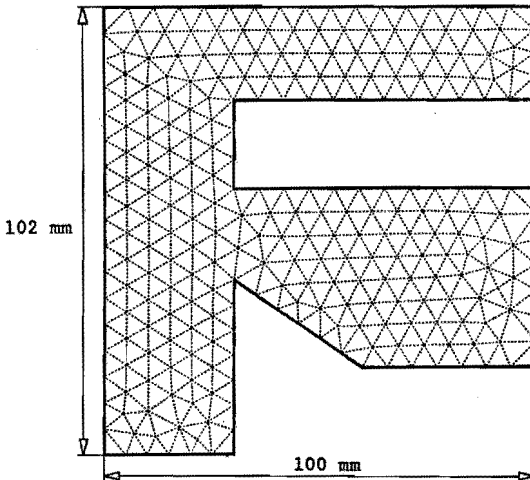is equal to 1.5 mm. A suitable element mesh is shown.

Fig. 6.2.1 Mesh of a cavity with sharp corners.

The experimental and numerical results, when the fluid is injected
through a single gate (with a volume flux of 10^{-7} m^3/s) are presented
in Fig. 6.2.2. The numerical analysis is performed in 63 incremental
time steps. After every increment the position of the flow front is
drawn. The experimental results are indicated by the heavy solid
lines. The computed flow fronts, of which the injection time cor-
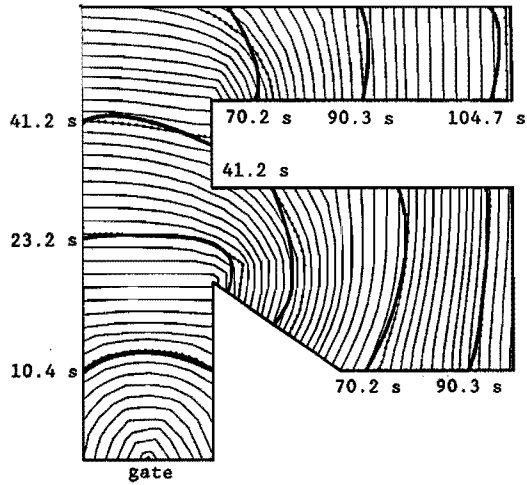responds to the experimentally determined flow fronts are marked by
dots.

Fig. 6.2.2 Experimentally and numerically obtained flow fronts in a geometry with a concave contour.

It should be noted that, for the experiments with glycerol (different from polymers) the surface tension had an influence on the flow near the boundaries, especially, if the radius of the flow front was small.
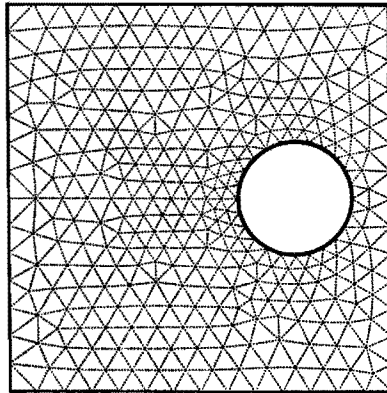

Fig. 6.2.3 Mesh of a cavity with a circular insert.

Particularly this occured with flow around corners. In order to reduce this effect, the cavity had to be wetted with glycerol before the experiment started.

Another experiment was carried out, using a cavity of 100x100x1.5 mm with a circular insert. Fig. 6.2.3 shows the finite element mesh.
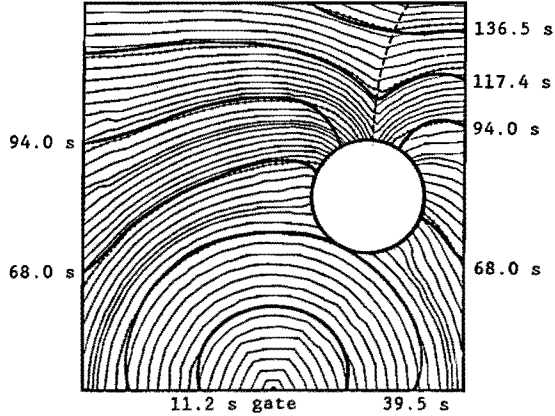

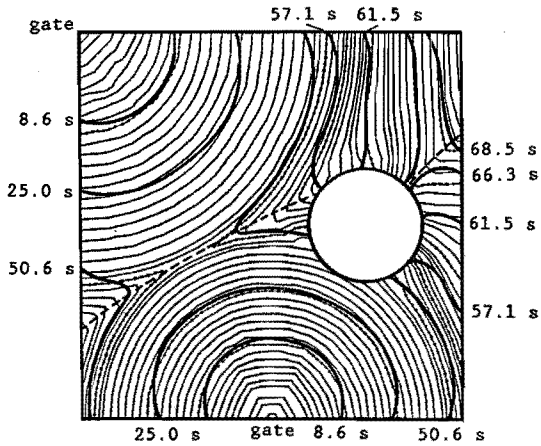Fig. 6.2.4 Flow fronts and weld line for one injection point.

Fig. 6.2.5 Flow fronts and weld lines for two injection points.

The experimental and numerical results, with one and two injection points, are given by Fig. 6.2.4 and Fig. 6.2.5, respectively. The volume flux for every injection point was equal to 10^{-7} m^3/s. The flow fronts are drawn after each increment. The numerically obtained flow fronts which correspond to the experimentally determined ones are indicated by dots again. The dashed curves represent the weld lines for the experimental cases.

Finally, filling of a rectangular cavity (158x38x0.35 mm) is simu-lated, containing two rectangular areas with a reduced gap of 0.2 mm (Fig. 6.2.6).
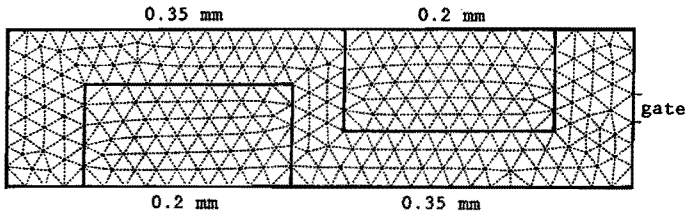

Fig. 6.2.6 Mesh of a cavity with sudden variations in height.

Krueger and Tadmor (1980) also used this configuration for their experiments. One of their experiments involved determination of the flow front when injecting corn syrup (Newtonian fluid), under iso-thermal conditions. Fig. 6.2.7 shows the result of this experiment along with the numerically obtained flow fronts (drawn after every increment). No indication of the injection time was available.
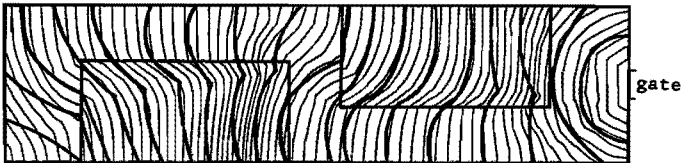

Fig. 6.2.7 Experimentally (Krueger and Tadmor, 1980) and numerically obtained flow fronts.

Within the thin film theory, full slip occurs along the boundaries of the cavity. In the experimental situation the no-slip condition is

imposed instead. The influence of this approximation on the progress
of the flow front could not be investigated properly, because as
stated before, the surface tension played a role too.
However, from the results above, it can be concluded that, in the
case of an isothermal Newtonian flow, determination of the flow
fronts and weld lines for various cavities can be performed satisfac-
torily.

6.3   Examination of the influence of material parameters on the
       injection pressure and maximum solidified layer thickness, as
       well as, the accuracy of the temperature approximation

A number of calculations are carried out, to simulate the filling of
a centre gated disk, size Φ200x2 mm, in order to investigate the
influence of some material properties on the pressure at the gate and
the maximum thickness of the solidified layer. Also, the accuracy of
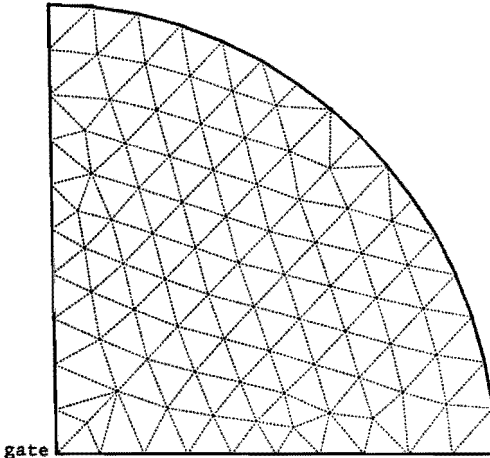estimating the temperature is examined.

gate

Fig. 6.3.1 Finite element mesh of a quarter disk.

The mesh, with three node elements that is used for all of the
simulations is shown in Fig. 6.3.1.

Influence of material properties

For the simulations, the viscosity is described by the Carreau model
according to (4.2.3), i.e.

$$\eta = B_1 \exp(A_1/T)[1 + (B_2 \exp(A_2/T)\dot{\gamma})^2]^{(n-1)/2} \tag{6.3.1}$$

The specific volume ν as a function of the pressure p and the tem-
perature T is approximated by

$$\nu = \nu_o + a(p - p_o) + b(T - T_o) \tag{6.3.2}$$

The solidification temperature T_s as a function of the pressure p
reads

$$T_s = T_o + c(p - p_o) \tag{6.3.3}$$

A_1	=	$1.444*10^4$		K
B_1	=	$6.845*10^{-9}$		Pas
A_2	=	$1.312*10^4$		K
B_2	=	$5.050*10^{-13}$		1/s
n	=	0.1	- 0.4	
ν_o	=	10^{-3}		m^3/kg
p_o	=	0		Pa
T_o	=	418		K
a	=	$-1.5*10^{-12}$	- $0.0*10^{-12}$	$m^3/(kgPa)$
b	=	$0.0*10^{-6}$	- $1.5*10^{-6}$	$m^3/(kgK)$
c	=	$0.0*10^{-6}$	- $0.9*10^{-6}$	K/Pa
λ	=	0.1	- 0.3	J/(smK)
c_p	=	2000		J/kg
Γ	=	2250		J/kg

Table 6.3.1 Physical properties of the model fluid.

The material parameters of (6.3.1), (6.3.2) and (6.3.3) and the
remaining physical properties (all based on Makrolon 6560) are listed
in Table 6.3.1. It is assumed that p, T and $\dot{\gamma}$ are expressed in Pa, K
and 1/s, respectively, that with respect to (6.3.1) - (6.3.3).
The polymer is injected at a temperature of 523 K. The walls of the
mould are kept at a temperture of 323 K and the total injection time
equals 1 s.
The injection pressure and the maximum solidified layer thickness are
influenced by the heat conduction coefficient λ, the power law ex-
ponent n, the coefficients a and b in the expression for the specific
volume and the coefficient c in the relation for the solidification
temperature. These specific contributions are investigated separate-
ly.
Fig. 6.3.2 shows the influence of the heat conduction coefficient λ
on the injection pressure and the maximum solidified layer thickness
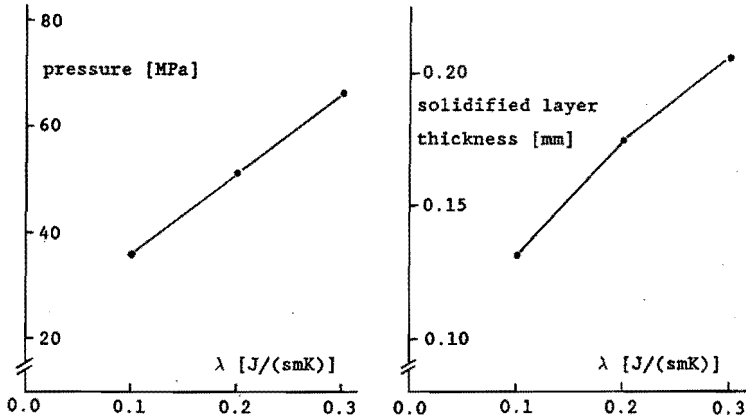at the end of the filling stage.

Fig. 6.3.2 The influence of the heat conduction coefficient λ,
for n = 0.4, a = 0 [m³/(kgPa)] and b = 0 [m³/(kgK)],
and c = 0 [K/Pa].

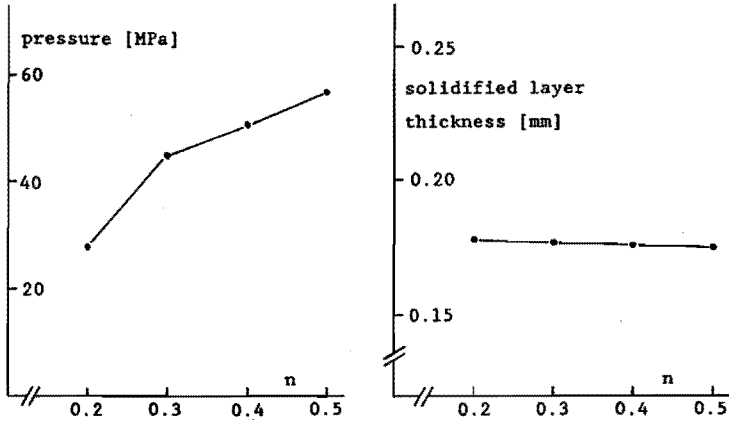In Fig. 6.3.3 the influence of the power law exponent n on the same
quantities is displayed.

Fig. 6.3.3 The influence of the power law exponent n, for
$\lambda = 0.2$ [J/(smK)], $a = 0$ [m^3/(kgPa)],
$b = 0$ [m^3/(kgK)] and $c = 0$ [K/Pa].

The dependence of the pressure and the maximum solidified layer
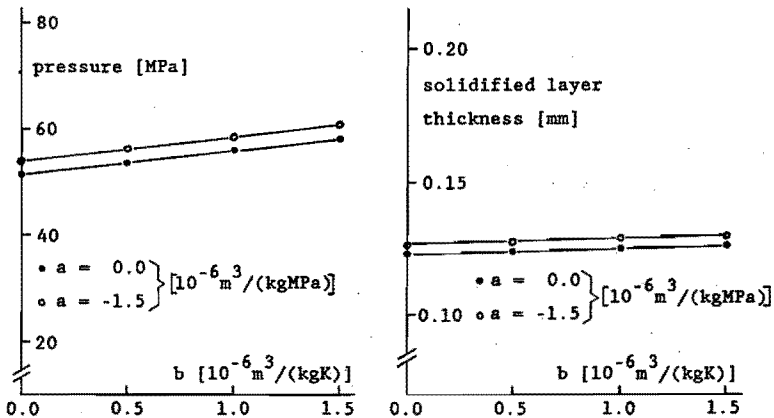thickness on the coefficients a and b is sketched in Fig. 6.3.4.

Fig. 6.3.4 The influence of the coefficients a and b, for
$\lambda = 0.2$ [J/(smK)], $n = 0.4$ and $c = 0$ [K/Pa].

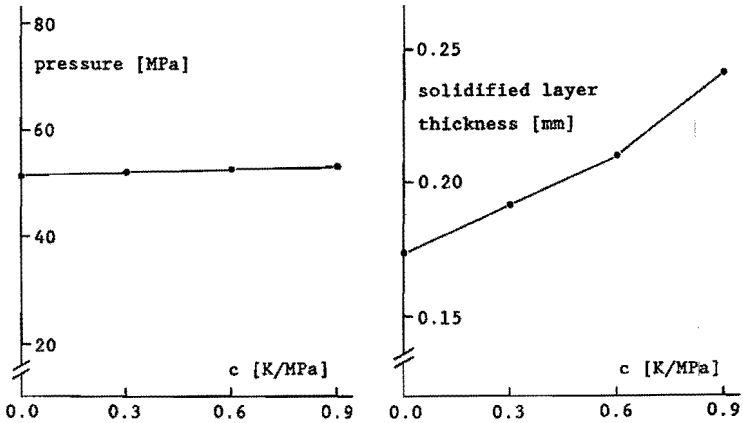The influence of the coefficient c is presented in Fig. 6.3.5.

Fig. 6.3.5 The influence of the coefficient c, for
$\lambda = 0.2$ [J/(smK)], $n = 0.4$, $a = 0$ [m^3/(kgPa)] and
$b = 0$ [m^3/(kgK)].

It can be concluded that reliable experimental data are required for
n and especially for λ. Also, the influence of the parameter b on the
injection pressure is considerable and it is worth taking into ac-
count. The parameter c only influences the solidified layer thick-
ness.

The accuracy the temperature calculation

The injection time for the simulations described in the first part of
this Paragraph is 1 s, in which case the core temperature decreased
about 4K, as a function of the radius. The temperature distribution
is rotationally symmetric within an accuracy of about 0.2 K.
If a longer injection time is chosen, the temperature fall increases.
In Fig. 6.3.6, two simulations, are compared filling a disk in 3 s,
using a Newtonian fluid (a) and a Carreau fluid (b). The physical
properties chosen are: $\lambda = 0.2$ J/(smK); $n = 0.4$; $\nu = 10^{-3}$ m^3/kg;
$T_s = 0$ K (no solidification is taken into account). The remaining
data are presented in Table 6.3.1. The viscous dissipation term in
the energy equation is left out of both simulations. This figure
shows the isotherms at the midplane. The temperature is a decreasing

function of the distance from the gate to the flow front. The dif-
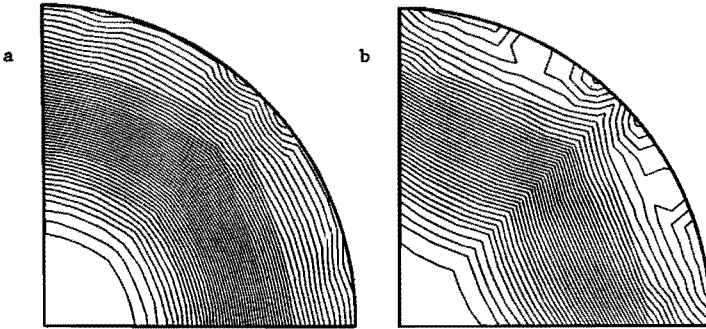ference between two adjacent contours is 1 K.

Fig. 6.3.6 Temperature distribution on the midplane at the end
of the filing stage, for a Newtonian fluid (a) and
for a Carreau fluid (b).

It should be noted that the symmetry in case b is disturbed. This is
caused by an inaccurate evaluation of the convective part $\vec{v}^* \cdot \vec{\nabla}^* T$
(equation (5.5.1)) in the energy equation. The result could not be
improved by a higher order approximation (three point backwards) of
$\vec{\nabla}^* T$. For that reason it can be concluded that the problem probably is
originated by the approximation of $\vec{v}^*$, which is proportional to $\vec{\nabla}^* p$,
according to (5.3.6). Using a finer mesh and/or a higher order
element (parabolic instead of linear) could not reduce the problem,
because $\vec{\nabla}^* p$ remains discontinuous across the element sides. This
again leads to the suggestion that an element has to be formulated
with at least $\vec{\nabla}^* p$ continuity across the element edges.

6.4   Non-isothermal non-Newtonian flow in a rectangular mould

Filling of a rectangular mould is simulated, using a length, width
and height of 300, 75 and 2 mm, respectively. The same dimensions
were used in the experiments, by Wales, Van Leeuwen and Van der Vijgh
(1973), the polymer was injected across the entire width of the mould
through a line gate. The physical properties of the polystyrene used

are listed in Table 6.4.1. T and $\dot{\gamma}$ are expressed in K and 1/s, respectively.

$\eta = 6700\exp(- 0.017(T - 493))\dot{\gamma}^{0.356-1}$ Pas

$\lambda = 0.1295$ J/(smK)

$\nu = 0.9434*10^{-3}$ m^3/kg

$c_p = 1733$ J/(kgK)

$T_s = 373$ K

$\Gamma = 3400$ J/kg

Table 6.4.1 Physical properties of PS 678 DOW.

The viscosity η as a function of the shear rate $\dot{\gamma}$ is described by the power law model. For the temperature dependence of η, an approximation of the Arrhenius equation is used. The thermodynamical properties λ, ρ and c_p, have the same constant values in the solid as in the liquid phases. Also, the solidification temperature T_s and the transition heat Γ are assumed to be constant. Van Wijngaarden, Dijksman and Wesseling (1982) also used similar material properties for their calculations, based on the analysis of the two-dimensional flow of a molten polymer.

Filling is simulated for two different volume fluxes of $18*10^{-6} m^3$/s and $540*10^{-6} m^3$/s. The average velocity of the flow front in these cases is 0.12 m/s and 3.6 m/s, respectively. It should be noted that experimental data for only the low flow rate are available. The polymer is injected into the mould, at a temperature of 523 K, the walls of the mould are kept at a temperature of 323 K. The mould, in the numerical analysis, is filled at such time intervals that the flow front progresses in steps of approximately 6 mm. In Fig. 6.4.1, the finite element mesh used (three node elements) and the flow fronts predicted are presented, for the average velocity equal to 0.12 m/s (a) and equal to 3.6 m/s (b). Near the gate the mesh is finer because, in that region, the temperature gradients in flow direction near the walls are relatively large.

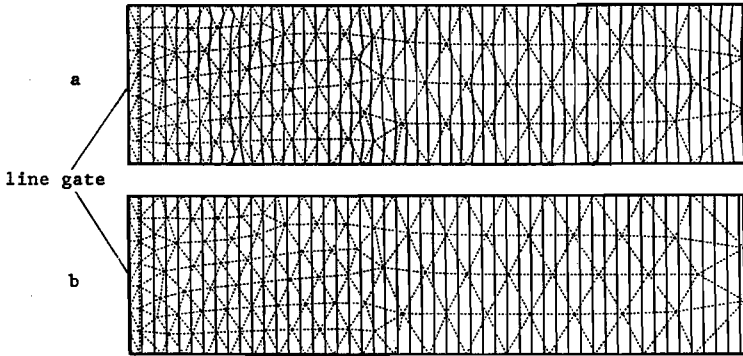Fig. 6.4.1 Finite element mesh and the flow fronts due to an
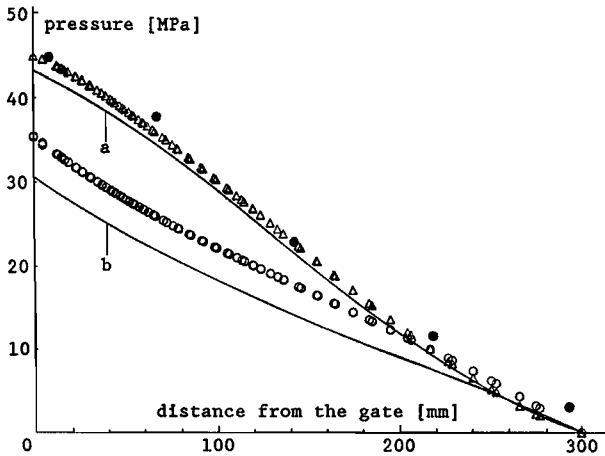average flow velocity of 0.12 m/s (a) and 3.6 m/s
(b), respectively.

Fig. 6.4.2 Pressure distribution along the length axis of the
mould, at the end of the filling stage. Measurements
from Wales et al. (1973) for case a (●). Calcula-
tions from Van Wijgaarden et al. (1982) for cases a
and b (solid lines). Present results for cases a (△)
and case b (o).

Fig. 6.4.2 shows the pressure distribution along the length axis of the mould when the mould has just been filled. Every symbol (o,Δ) represents a nodal pressure. The measurements by Wales et al. and the numerical results of Van Wijngaarden et al., are displayed also. It should be noted that the experimentally obtained pressure at the end of the cavity distinctly exceeded zero. Probably the packing stage had already started. In order to make a proper comparison possible, the experimental pressures have to be corrected downwards by this amount. Furthermore, it should be mentioned that the difference between the results of Van Wijngaarden et al. and the present results are most pronounced for high injection velocities and is caused by the difference between the flow front models used. The thickness of the solidified layer at various times and related to a flow velocity of 0.12 m/s, is displayed in Fig. 6.4.3.
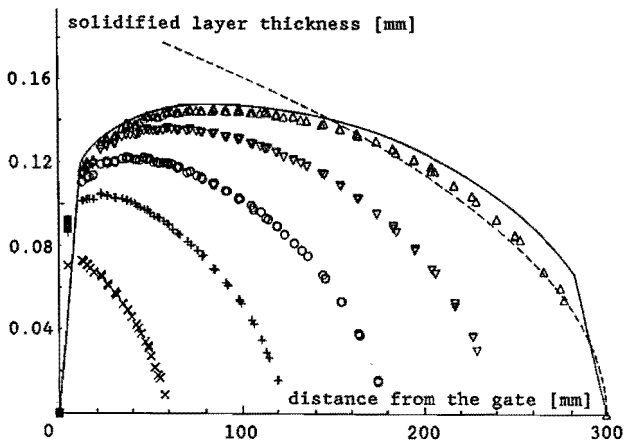
Fig. 6.4.3 Growth of the solidified layer as a function of time and position for case a. Calculation of Van Wijngaarden et al. (1982) for t = 2.50 s (——). Present results for t = 0.50 s (x), t = 1.03 s (+), t = 1.49 s (o), t = 2.00 s (∇) and t = 2.50 s (Δ). Growth according to the penetration theory (---).

The calculated solidified layer thickness according to the penetra-
tion theory proposed by Janeschitz-Kriegl (1979) and Dietz and White
(1978) is indicated too. It can be seen that the solid-liquid inter-
face according to the present theory approaches the curve obtained by
the penetration theory which can be considered as an upper limit. The
improvement compared with the analysis of Van Wijngaarden et al. can
be explained with the flow front model (Appendix 4).
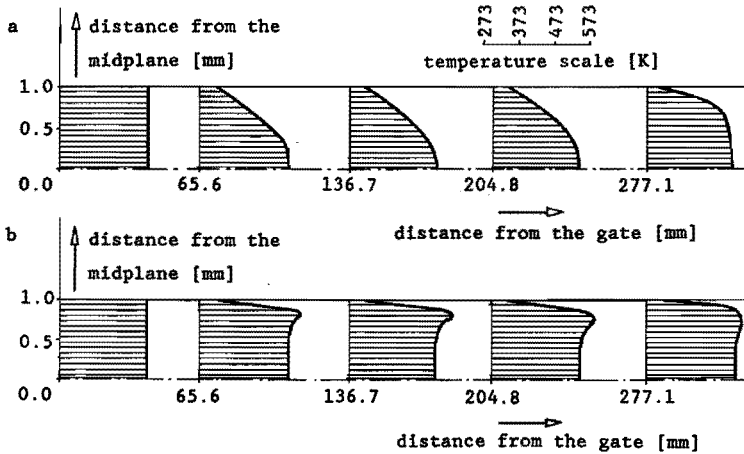
Fig. 6.4.4 Temperature profiles at the end of the filling
stage.

The temperature distribution along the axis of the mould at the end
of the filling stage has been drawn in Fig. 6.4.4 and indicated with
a and b, for injection velocities of 0.12 m/s and 3.6 m/s, respec-
tively. Note that, for the case b the polymer is heated locally, due
to the large contribution of the viscous dissipation during injec-
tion. The temperature peak occurs at the position of the maximum
shear rate, of course.

6.5   The non-isothermal filling of a complex mould with a non-
      Newtonian fluid

In this Paragraph, a comparison will be made between the experimental
flow pattern in a mould and the numerical simulation, where the non-
Newtonian flow is considered under non-isothermal conditions. In the
mould, a rectangular box is produced with a varying wall thickness.
The flow pattern is registered for a number of short shots with ABS.
These experiments were carried out by DSM (Kersemakers, 1987).

Geometry

The box, with a gate in the centre, has two planes of symmetry.
Assuming that the process conditions are symmetrical with respect to
these planes, only a fourth part of the box can be considered. Fig.
6.5.1 shows a quarter of the geometry with its important dimensions.
The geometry is divided into 4 sub-areas (A to D). Sub-area A has a
constant wall thickness, but the other sub-areas have linearly vari-
able wall thicknesses. For adjacent sub-areas the thickness shows a
discontinuity.
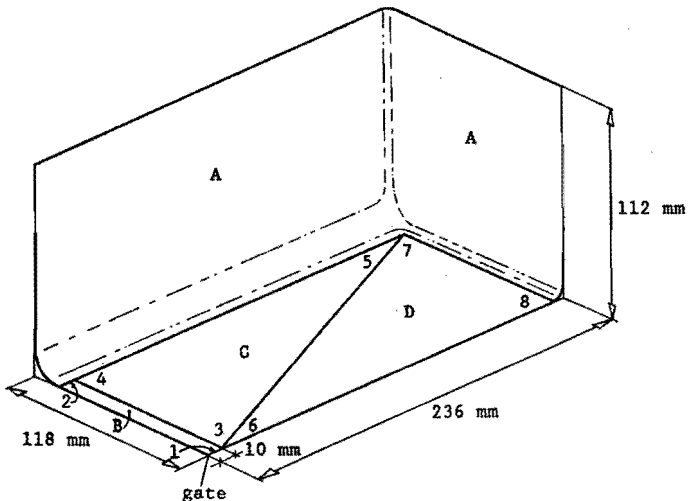
Fig. 6.5.1 Quarter of the experimental mould.

Table 6.5.1 includes the side thicknesses (1 and 2) and at the points (3 to 8) of the sub-areas.

Sub-area	point/side	wall thickness (mm)
A	-	3.50
B	1	2.75
	2	3.05
C	3	2.90
	4	3.00
	5	4.20
D	6	3.80
	7	4.20
	8	4.00

Table 6.5.1 Wall thicknesses of the various sub-areas.

Fig. 6.5.2 Finite element mesh.

Physical properties

The mould is injected with ABS (Ronfalin FF 50). A curve fit for the experimental viscosity data (measured on a Reograph 2001 apparatus) can be made using the three parameter power law model according to (4.2.4), i.e.

$$\eta = B \ exp(\frac{A}{T})\dot\gamma^{n-1} \qquad (6.5.1)$$

For the specific volume the p-ν-T diagram for ABS Novodur Typ PMT (Kenndaten: Rheologie, 1982) is used. Since ABS is an amorphous polymer it i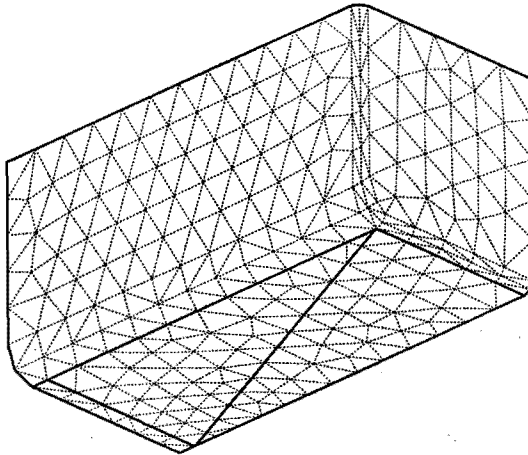s quite easy to fit a curve for ν as a function of p and T. Both in the liquid and the solid phases the following approximation is made.

$$\nu = a \ exp(b(p - p_o)) + c(T - T_o)exp(d(p - p_o)) \qquad (6.5.2)$$

with adjustments of the parameters a, b, c, and d in the solid and liquid phases separately. The solidification temperature T_s as a function of the pressure can be approximated quite well by a straight line, in the pressure range which is of interest for the injection moulding process under consideration.

$$T_s = T_o + \alpha(p - p_o) \qquad (6.5.3)$$

The proportionality factor is indicated by α. No measurements for the heat capacity c_p as a function of the temperature T for ABS were available. Therefore, as a compromise the almost identical diagram for polystyrol was used (Kenndaten: Thermodynamik, 1979). In the solid and the liquid regions the c_p curve is straight but has a different slope. The small peak in the transition area of the curve is taken into account by a small amount of fusion heat Γ, which is released at T_s. With a shift of T_s as a function of pressure (6.5.3), it can be derived that

$$c_p = g + h(T - T_o - \alpha(p - p_o)) \qquad (6.5.4)$$

The parameters, g and h, are different for the solid and the liquid phases.

The heat conduction coefficient is approximated too, by a linear function of the temperature. Using the same temperature shift as for the heat capacity c_p, λ can be written, for the entire temperature range, as

$$\lambda = r + s(T - T_o - \alpha(p - p_o)) \tag{6.5.5}$$

with, r and s being constants. The material parameters in the relations (6.5.1) - (6.5.5) are listed in Table 6.5.2.

A = 4050	K	
B = 4	Pas	
n = 0.375		
T_o = 373	K	
p_o = 10^5	Pa	
Γ = 2000	J/kg	
α = $5.4255*10^{-7}$	K/Pa	

	fluid phase	solid phase	
a =	$9.78*10^{-4}$	$9.78*10^{-4}$	m^3/kg
b =	$-3.86*10^{-10}$	$-2.78*10^{-10}$	1/Pa
c =	$5.53*10^{-7}$	$2.50*10^{-7}$	m^3/(kgK)
d =	$-4.30*10^{-9}$	$-3.74*10^{-9}$	1/Pa
g =	$1.865*10^3$	$1.555*10^3$	J/(kgK)
h =	3.44	4.47	J/(kgK^2)
r =	$1.75*10^{-1}$	$1.75*10^{-1}$	J/(smK)
s =	$-1.20*10^{-4}$	$-1.20*10^{-4}$	J/(smK^2)

Table 6.5.2 Parameters of the curve fits for the physical properties of ABS.

Process conditions

The polymer is injected at a temperature of 503 K. The walls of the mould are kept at a temperature of 323 K. The total injection time equals 2.8 s.

Short shots versus calculated flow fronts

Fig. 6.5.3 displays the calculated flow fronts and a number of short shots.

The pressure contours are displayed in Fig. 6.5.4, the pressure is a decreasing function of the distance from the gate to the flow front, the difference between two adjacent contours equals 1.3 MPa. The total injection pressure is equal to 49.5 Mpa.
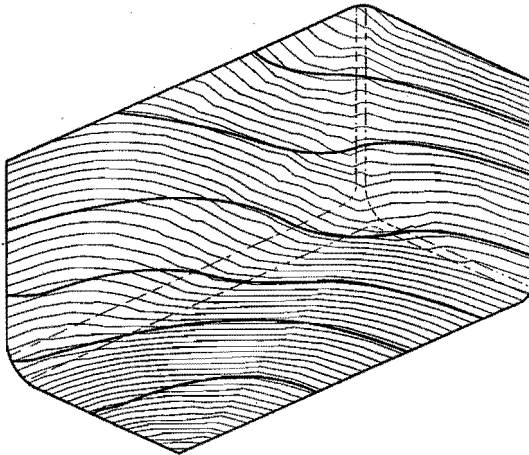
Fig. 6.5.3 Numerical and experimental (heavy solid lines) flow
fronts for the non-isothermal non-Newtonian case.

When an isothermal simulation is carried out with a Newtonian fluid (in order to reduce the computational effort), the flow fronts produced are shown in Fig. 6.5.5.

It should be noted that an isothermal Newtonian filling simulation is not suffficient, for an accurate approximation of the flow front.
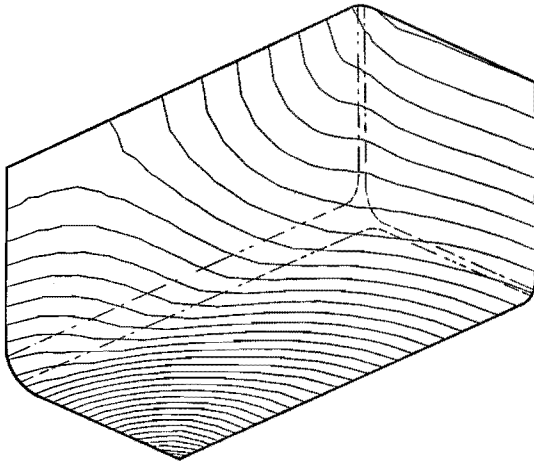
Fig. 6.5.4 Calculated pressure contours for the non-isothermal
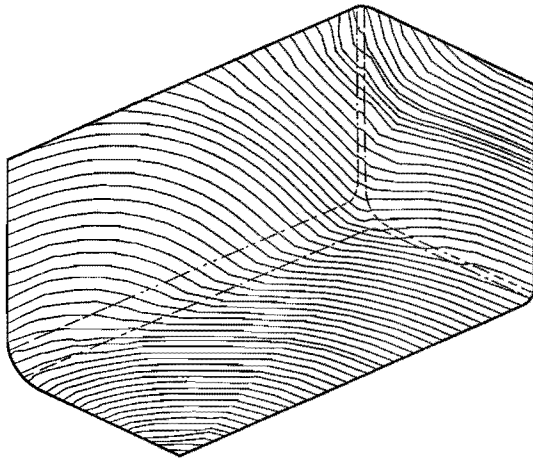non-Newtonian case.

Fig. 6.5.5 Isothermal simulation with a Newtonian fluid.

7   CONCLUSIONS

7.1   Discussion and recommendations

A general continuum approach, which deals with discontinuity surfaces
supplies not only the local balance equations, but also, the jump
relations at the solid-liquid interfaces, which are valid irrespec-
tive of the material (amorphous or semi-crystalline polymers). There-
fore the jump relations should be regarded as a basis for describing
all the phenomena that take place at these surfaces.

The importance of the velocity component in the direction of the
channel height could not be investigated, because evaluating this
component could not be done accurately enough. This inaccuracy is
originated by the determination of the pressure gradient in the
vertices of the elements. It can be assumed that this is also the
reason for the inaccurate evaluation of the decrease in temperature
in the core of the flow, when long injection times are used.
The pressure gradient is discontinuous across the element edges. In
order to evaluate this quantity in a vertex node, a weighted average
is applied over all the elements containing the vertex. Several
weighting methods are tested (with a weighting factor proportional to
the subtended element angle, or reversely proportional to the dis-
tance to the centroid of the element, or proportional to the element
area, etc.), but no method could improve the results. Also, refining
the finite element mesh and applying a higher order element (parabol-
ic instead of linear) could not solve the problem. This leads to the
suggestion that an element has to be formulated with, at least,
continuity of the pressure gradient across the element sides.

The flow front tracing technique proposed in Paragraph 5.2 appears to
be satisfactory. The intersections of the flow front with the element
edges are the only points of the flow front that are calculated. If
the used mesh is coarse, the flow front is composed of a number of
rather long line segments. Distinctly curved flow fronts (when two
flow fronts have just met) cannot be traced accurately. Therefore, it

is desirable, to calculate for every element that is involved by the flow front, at least one internal point, which approximately doubles the total number of line segments of the flow front.

The fountain flow model suggested in Appendix 4 is very simple, but it needs improvement. Therefore, the two-dimensional fountain flow problem (filling a rectangular duct) has to be examined numerically. For the isothermal case, this has been done already for different viscosity models (Crowet, Dierieck, 1983; Mavridis, Hrymak, Vlachopoulos, 1986). However, for predicting the solidified layer growth and temperature development in the bulk of the flow, it is essential to have a reliable picture of the phenomena at the flow front.

Before a better analytical model for the temperature distribution can be developed, firstly, it is necessary to solve the non-Newtonian non-isothermal fountain flow problem with numerical techniques.

The effect of undercooling occurring for semi-crystalline polymers is not taken into account (see Paragraph 2.7). In that case, the solidification rate depends largely on the crystal growth rate and local shear effects. The recent work of Janeschitz-Kriegl and coworkers (1983, 1984 and 1987) offers a good starting point for approaching this problem.

This research work is confined to viscous flow, in spite of the substantial viscoelastic effects that occur in polymer melts. Therefore, additional work with respect to these effects is desirable. A first step will be the computation of elastic stresses assuming that flow in the cavity can determined completely from the viscous forces only. The elasticity is added afterwards, by using the calculated viscous deformation in a viscoelastic model. This approximation has to be checked by (numerical) experiments. Finally, the full set of equations that govern viscoelastic flow has to be solved. However, for the time being, this goal is unattainable, because of the large computational times and the number of difficulties still to be overcome in this field.

Appendix 1: <u>Transport theorem formulations</u>

A three-dimensional time dependent volume V(t) is considered in
which, a continuous and sufficiently differentiable scalar or vector
quantity $\phi(\vec{x},t)$ can be defined ($\vec{x}$ being the position vector of a
spatial point of the volume).

The rate of change of the following volume integral

$$\Phi(t) = \int\limits_{V(t)} \phi(\vec{x},t)dV \qquad (A1.1)$$

is defined as

$$\frac{d\Phi(t)}{dt} = \lim_{\Delta t \to 0} \frac{1}{\Delta t}[\int\limits_{V(t+\Delta t)} \phi(\vec{x},t+\Delta t)dV - \int\limits_{V(t)} \phi(\vec{x},t)dV] \qquad (A1.2)$$

If the time interval Δt approaches zero, the volume integral with
respect to V(t+Δt) can be replaced by a volume integral over V(t) and
a surface integral over the closure A(t) of the volume. The surface
has a unit normal vector $\vec{n}$, which points out the volume. The normal
velocity of the surface equals $\vec{u}$. Relation (A1.2) transforms into

$$\frac{d\Phi(t)}{dt} = \lim_{\Delta t \to 0} \frac{1}{\Delta t}[\int\limits_{V(t)} \phi(\vec{x},t+\Delta t)dV + \Delta t \int\limits_{A(t)} \phi(\vec{x},t+\Delta t)\vec{u}\cdot\vec{n}dA +$$

$$- \int\limits_{V(t)} \phi(\vec{x},t)dV]=$$

$$= \int\limits_{V(t)} \lim_{\Delta t \to 0} \frac{1}{\Delta t}[\phi(\vec{x},t+\Delta t) - \phi(\vec{x},t)]dV +$$

$$+ \int\limits_{A(t)} \lim_{\Delta t \to 0} \phi(\vec{x},t+\Delta t)\vec{u}\cdot\vec{n}dA \qquad (A1.3)$$

With the introduction of the spatial time derivative it simply fol-
lows that

$$\frac{d\Phi(t)}{dt} = \int\limits_{V(t)} \frac{\partial\phi(\vec{x},t)}{\partial t}dV + \int\limits_{A(t)} \phi(\vec{x},t)\vec{u}\cdot\vec{n} \, dA \qquad (A1.4)$$

Relation (A1.4) is only valid if $\phi(\vec{x},t)$ is continuous in $V(t)$. If, in $V(t)$, a time dependent surface $A_d(t)$ is present, where $\phi(\vec{x},t)$ changes discontinuously (such a surface will be called a discontinuity surface), the spatial time derivative of $\phi(\vec{x},t)$ does not exist everywhere in the volume $V(t)$. The transport theorem (A1.4) has to be adjusted. The surface $A_d(t)$ will cut volume $V(t)$ into two parts, $V^a(t)$ and $V^b(t)$, with surfaces $A^a(t)$ and $A_d(t)$, and $A^b(t)$ and $A_d(t)$, respectively. The normal velocity of $A^a(t)$ and $A^b(t)$ is equal to $\vec{u}$. The discontinuity surface, with a unit normal $\vec{n}_d$ pointing from $V^a(t)$ into $V^b(t)$, moves with the normal velocity $\vec{u}_d$. Relation (A1.4) is separately valid for volume $V^a(t)$ with surfaces, $A^a(t)$ and $A_d(t)$, and for volume $V^b(t)$ with surfaces, $A^b(t)$ and $A_d(t)$.
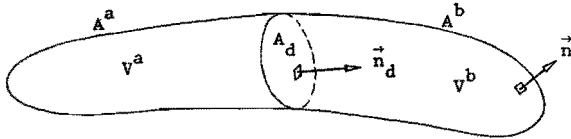
Fig. A1.1 Material volume, cut by a discontinuity surface.

Without further mentioning of the independent variables $\vec{x}$ and t, the rate of change of $\Phi(t)$ can be written as

$$\frac{d\Phi(t)}{dt} = \int_{V^a}\frac{\partial\phi}{\partial t}dV + \int_{V^b}\frac{\partial\phi}{\partial t}dV + \int_{A^a}\phi\vec{u}\cdot\vec{n}dA + \int_{A^b}\phi\vec{u}\cdot\vec{n}dA +$$

$$- \int_{A_d}(\phi^b - \phi^a)\vec{u}_d\cdot\vec{n}_d dA \qquad (A1.5)$$

Where ϕ^a and ϕ^b are the values of ϕ at the sides a and b of the discontinuity surface.

Relations (A1.4) and (A1.5) are the transport theorems for not material bounded volumes, without or with a discontinuity surface, respectively.

For material bounded volumes, $\vec{u}\cdot\vec{n}$ can be replaced by $\vec{v}\cdot\vec{n}$, with $\vec{v}$ the material velocity. The transport theorem for volumes without a discontinuity surface reads

$$\frac{d\Phi(t)}{dt} = \int_V \frac{\partial\phi}{\partial t}dV + \int_A \phi\vec{v}\cdot\vec{n}dA \tag{A1.6}$$

With the theorem of Gauss, this relation can be transformed to

$$\frac{d\Phi(t)}{dt} = \int_V [\frac{\partial\phi}{\partial t} + \vec{\nabla}\cdot(\vec{v}\phi)]dV \tag{A1.7}$$

With the definition of the material time derivative $\dot{\phi} = \frac{\partial\phi}{\partial t} + \vec{v}\cdot\vec{\nabla}\phi$ (A1.7) can be rewritten as

$$\frac{d\Phi(t)}{dt} = \int_V (\dot{\phi} + \phi\vec{\nabla}\cdot\vec{v})dV \tag{A1.8}$$

The transport theorem for material bounded volumes, with a discontinuity surface, can be written according to

$$\frac{d\Phi(t)}{dt} = \int_{V^a+V^b} \frac{\partial\phi}{\partial t}dV + \int_{A^a+A^b} \phi\vec{v}\cdot\vec{n}dA - \int_{A_d}(\phi^b - \phi^a)\vec{u}_d\cdot\vec{n}_d dA \tag{A1.9}$$

With the theorem of Gauss (A1.9) this becomes

$$\frac{d\Phi(t)}{dt} = \int_{V^a+V^b} [\frac{\partial\phi}{\partial t} + \vec{\nabla}\cdot(\vec{v}\phi)]dV - \int_{A_d}[\phi(\vec{u}_d - \vec{v})]_d\cdot\vec{n}_d dA \tag{A1.10}$$

where the bracket notation $[\phi(\vec{u}_d-\vec{v})]_d$ with subscript d expresses $\phi^b(\vec{u}_d-\vec{v}^b) - \phi^a(\vec{u}_d-\vec{v}^a)$. With the introduction of the material time derivative of ϕ, relation (A1.10) can be rewritten as

$$\frac{d\Phi(t)}{dt} = \int_{V^a+V^b} (\dot{\phi} + \phi\vec{\nabla}\cdot\vec{v})dV - \int_{A_d}[\phi(\vec{u}_d - \vec{v})]_d\cdot\vec{n}_d dA \tag{A1.11}$$

Equations (A1.7) and (A1.8) are the transport theorems for material volumes, without a discontinuity surface. Equations (A1.10) and (A1.11) are the transport theorems for material volumes with a discontinuity surface.

Appendix 2: <u>Constitutive relations for $\overset{\bullet}{\varepsilon}$</u>

According to (2.7.6), $\varepsilon = \varepsilon(\rho,T)$. However, by interchanging the independent variable ρ by p_0, assuming that this relation is invertible, it can be written $\varepsilon = \varepsilon(p_0,T)$. The material time derivative $\overset{\bullet}{\varepsilon}$ can equivalently be written as

$$\overset{\bullet}{\varepsilon} = (\frac{\partial \varepsilon}{\partial T})_\rho \overset{\bullet}{T} + (\frac{\partial \varepsilon}{\partial \rho})_T \overset{\bullet}{\rho} \quad ; \quad \overset{\bullet}{\varepsilon} = (\frac{\partial \varepsilon}{\partial T})_{p_0} \overset{\bullet}{T} + (\frac{\partial \varepsilon}{\partial p_0})_T \overset{\bullet}{p}_0 \qquad (A2.1)$$

Before the relations above are worked out, some important quantities, such as the heat capacities c_p and c_v, the isothermal compressibility κ_T and the equation of Gibbs, will be discussed. The heat capacities and the isothermal compressibility are defined by

$$c_v = (\frac{\partial \varepsilon}{\partial T})_\rho \quad ; \quad c_p = (\frac{\partial h}{\partial T})_{p_0} \quad ; \quad \kappa_T = \frac{1}{\rho}(\frac{\partial \rho}{\partial p_0})_T \qquad (A2.2)$$

In the second equation, h is the specific enthalpy defined by

$$h = \varepsilon + \frac{p_0}{\rho} \qquad (A2.3)$$

The entropy s and the pressure p_0 according to (2.7.5) and (2.7.9) are

$$s = - \frac{\partial f}{\partial T} \quad ; \quad p_0 = \frac{\partial f}{\partial \rho} \rho^2 \qquad (A2.4)$$

The equation of Gibbs can be obtained by differentiating the first and second relations of (A2.4) to ρ and T, respectively, i.e.

$$(\frac{\partial s}{\partial \rho})_T = - \frac{1}{\rho^2}(\frac{\partial p_0}{\partial T})_\rho \qquad (A2.5)$$

Considering ρ and T as being independent variables, using $f = \varepsilon - Ts$, the first relations of (A2.2) and (A2.4) and the equation of Gibbs, the first expression of (A2.1) can be worked out as

$$\dot{\varepsilon} = c_v \dot{T} + [\frac{p_0}{\rho^2} - \frac{T}{\rho^2}(\frac{\partial p_0}{\partial T})_\rho]\dot{\rho} \tag{A2.6}$$

If c_v and p_0 are known as functions of ρ and T, the rate of change $\dot{\varepsilon}$ can be calculated from (A2.6).

If p_0 and T are the independent variables, the second relation of (A2.1) transforms with the definition of c_p and h according to (A2.2) and (A2.3), into

$$\dot{\varepsilon} = [c_p + \frac{p_0}{\rho^2}(\frac{\partial \rho}{\partial T})_{p_0}]\dot{T} + (\frac{\partial \varepsilon}{\partial p_0})_T \dot{p}_0 \tag{A2.7}$$

Relation (A2.6), with $\rho = \rho(p_0,T)$ can be worked out as

$$\dot{\varepsilon} = [c_v - \frac{T}{\rho^2}(\frac{\partial p_0}{\partial T})_\rho(\frac{\partial \rho}{\partial T})_{p_0} + \frac{p_0}{\rho^2}(\frac{\partial \rho}{\partial T})_{p_0}]\dot{T} +$$

$$+ [\frac{p_0}{\rho^2}(\frac{\partial \rho}{\partial p_0})_T - \frac{T}{\rho^2}(\frac{\partial p_0}{\partial T})_\rho(\frac{\partial \rho}{\partial p_0})_T]\dot{p}_0 \tag{A2.8}$$

Substitution of the identity

$$(\frac{\partial \rho}{\partial T})_{p_0} = - (\frac{\partial \rho}{\partial p_0})_T(\frac{\partial p_0}{\partial T})_\rho \tag{A2.9}$$

and the isothermal compressibility κ_T (A2.2) leads to

$$\dot{\varepsilon} = [c_v + \frac{T}{\rho}\kappa_T(\frac{\partial p_0}{\partial T})_\rho^2 + \frac{p_0}{\rho^2}(\frac{\partial \rho}{\partial T})_{p_0}]\dot{T} +$$

$$+ [\frac{p_0}{\rho^2}(\frac{\partial \rho}{\partial p_0})_T + \frac{T}{\rho^2}(\frac{\partial \rho}{\partial T})_{p_0}]\dot{p}_0 \tag{A2.10}$$

Comparing (A2.10) with (A2.7) supplies the following relations

$$c_p = c_v + \frac{T}{\rho}\kappa_T(\frac{\partial p_0}{\partial T})_\rho^2 \tag{A2.11}$$

$$(\frac{\partial \varepsilon}{\partial p_0})_T = \frac{p_0}{\rho^2}(\frac{\partial \rho}{\partial p_0})_T + \frac{T}{\rho^2}(\frac{\partial \rho}{\partial T})_{p_0} \tag{A2.12}$$

Using (A2.12), equation (A2.7) can be written as

$$\dot{\varepsilon} = [c_p + \frac{p_0}{\rho^2}(\frac{\partial \rho}{\partial T})_{p_0}]\dot{T} + [\frac{p_0}{\rho^2}(\frac{\partial \rho}{\partial p_0})_T + \frac{T}{\rho^2}(\frac{\partial \rho}{\partial T})_{p_0}]\dot{p}_0 \qquad (A2.13)$$

If c_p and ρ are known as functions of p_0 and T, the rate of change $\dot{\varepsilon}$ can be calculated from (A2.13).

Replacing the second and third terms in relation (A2.13) by $(p_0/\rho^2)\dot{\rho}$ gives a more useful relation for $\dot{\varepsilon}$

$$\dot{\varepsilon} = c_p\dot{T} + \frac{p_0}{\rho^2}\dot{\rho} + \frac{T}{\rho^2}(\frac{\partial \rho}{\partial T})_{p_0}\dot{p}_0 \qquad (A2.14)$$

This relation will be used.

Appendix 3: <u>Reformulation of the jump relations</u>

The jump relations according (2.2.4), (2.3.4) and (2.5.4) are

$$\rho^b(\vec{u}_d - \vec{v}^b)\cdot\vec{n}_d - \rho^a(\vec{u}_d - \vec{v}^a)\cdot\vec{n}_d = 0 \tag{A3.1}$$

$$\rho^b\vec{v}^b(\vec{u}_d - \vec{v}^b)\cdot\vec{n}_d - \rho^a\vec{v}^a(\vec{u}_d - \vec{v}^a)\cdot\vec{n}_d - (\vec{t}^b + \vec{t}^a) = \vec{0} \tag{A3.2}$$

$$\rho^b(\varepsilon^b + \tfrac{1}{2}\vec{v}^b\cdot\vec{v}^b)(\vec{u}_d - \vec{v}^b)\cdot\vec{n}_d - \rho^a(\varepsilon^a + \tfrac{1}{2}\vec{v}^a\cdot\vec{v}^a)(\vec{u}_d - \vec{v}^a)\cdot\vec{n}_d +$$

$$- (\vec{t}^b\cdot\vec{v}^b + \vec{t}^a\cdot\vec{v}^a) + (\vec{q}^b - \vec{q}^a)\cdot\vec{n}_d = 0 \tag{A3.3}$$

where $\vec{t}^b$ and $\vec{t}^a$ are equal to $-\sigma^b\cdot\vec{n}_d$ and $\sigma^a\cdot\vec{n}_d$, respectively.
Substitution of (A3.1) in (A3.2) and (A3.3) leads to

$$(\vec{v}^b - \vec{v}^a)\rho^b(\vec{u}_d - \vec{v}^b)\cdot\vec{n}_d - (\vec{t}^b + \vec{t}^a) = \vec{0} \tag{A3.4}$$

$$[\varepsilon^b - \varepsilon^a + \tfrac{1}{2}(\vec{v}^b - \vec{v}^a)\cdot(\vec{v}^b + \vec{v}^a)]\rho^b(\vec{u}_d - \vec{v}^b)\cdot\vec{n}_d - (\vec{t}^b\cdot\vec{v}^b + \vec{t}^a\cdot\vec{v}^a) +$$

$$+ (\vec{q}^b - \vec{q}^a)\cdot\vec{n}_d = 0 \tag{A3.5}$$

Combination of (A3.4) and (A3.5) gives

$$(\varepsilon^b - \varepsilon^a)\rho^b(\vec{u}_d - \vec{v}^b)\cdot\vec{n}_d + (\vec{v}^b - \vec{v}^a)\cdot\frac{\vec{t}^a - \vec{t}^b}{2} +$$

$$- (\vec{q}^b - \vec{q}^a)\cdot\vec{n}_d = 0 \tag{A3.6}$$

The jump relations (A3.1), (A3.4) and (A3.6) are equivalent to the
original equations and will be used, however, in (A3.4) and (A3.6),
$\vec{t}^b$ and $\vec{t}^a$ are replaced by $-\sigma^b\cdot\vec{n}_d$ and $\sigma^a\cdot\vec{n}_d$, respectively.

Appendix 4 : <u>The fountain flow model</u>

If a grid line enters the fluid, an estimation of the distribution in
the z directions of some important quantities (ρ, T) can be made,
using a simple fountain flow model. In Fig. A4.1, the flow front
including the solidified layers against the walls for a real situa-
tion, as well as, for the used model are presented.


```
      v                        v                        v
       a                        a                        a
solidified layer
fluid layer
```

real situation   model   velocity profile
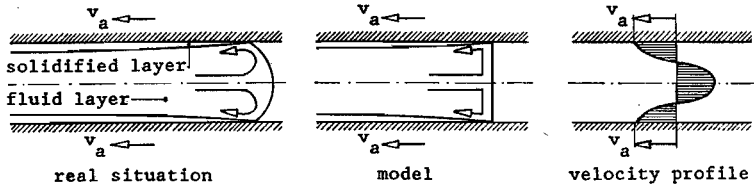
Fig. A4.1 The flow front for a realistic situation and for the
used model.

In order to get a better picture of the fountain effect, the mould is
assumed to have a velocity of v_a, so that the flow front remains
spatially fixed. In Fig. A4.1, a possible velocity profile $\vec{v}^*$ has
been drawn. Due to the no-slip conditions at the walls, material from
the centre of the flow will be transported towards the walls. The
particles moving with a velocity identical to the velocity of the
flow front, will remain at the same z position.

distribution
before (+++++)
after   (———)
the flow front
has passed

path of a particle

some distribution

velocity profile
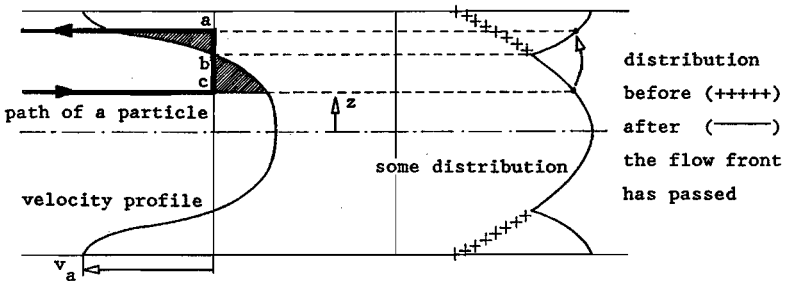
Fig. A4.2 The path of a particle.

With the assumption that the volume fluxes per unit of length through
the line segments ab and bc (as indicated in Fig. A4.2) are equal,

the path of a particle can be calculated (the shaded parts have the same area). If it is accepted that the properties of a particle do not change during the moment the particle is influenced by the fountain flow, the distributions over the channel height of certain quantities can be estimated. However for applications, where the length of the trajectory of a particle is important, the fountain flow model proposed here, needs adaptation.

References

- Bathe, K.J., Wilson, E.L.: "Numerical methods in finite element analysis", Prentice-Hall, (1976).
- Becker, E., Bürger, W.: "Kontinuumsmechanik", Teubner, Stuttgart, (1975).
- Bedford, A.: "Hamilton's principle in continuum mechanics", Pitman, Guildford, (1985).
- Bird, R.B., Armstrong, A.C., Hassager, O.: "Dynamics of Polymeric Liquids", Wiley, New York (1987).
- Bonnerot, R., Jamet, P.: "Numerical Computation of the Free Boundary for the Two-Dimensional Stefan Problem by Space-Time Finite Elements", J. of Comp. Physics, 25 (1977) 163-181.
- Carslaw, H.S., Jaeger, J.S.: "Conduction of Heat in Solids", Oxford University Press (1959).
- Cogswell, F.N.: "Polymer melt rheology: a guide for industrial practice", Wiley, New York, (1981).
- Couniot, A., Crochet, M.J.: "Finite elements for the numerical simulation of injection molding", Proceedings of the NUMIFORM '86 Conference, Gothenburg, (1986) 165-170.
- Crowet, F., Dierieck, C.: "Stream function formulation of the 2-d Stokes problem in a multiple-connected domain", J. Mécanique Théorique Appliquée, 2 (1983) 67-74.
- Dietz, W., White, J.L.: "Ein einfaches Modell zur Berechnung des druckverlustes während des Werzeugfüllvorganges und der eingefrorenen Orientierung beim Spritzgiessen amorpher Kunststoffe", Rheol. Acta, 17 (1978) 676-692.
- Dietz, W., White, J.L., Clark, E.S.: "Orientation Development and Relaxation in Injection Molding of Amorphous Polymers", Polym. Eng. and Sci., 18(4) (1978) 273-277.
- Dijksman, J.F., Savenije, E.P.W.: "The flow of Newtonian and non-Newtonian liquids through annular converging regions", Rheol. Acta, 24 (1985) 105-118.
- Eder, G., Janeschitz-Kriegl, H.: "Stefan Problem and Polymer Processing", Polym. Bull., 11 (1984) 93-98.

- Ferry, J.D.: "Viscoelastic Properties of Polymers", Wiley, New York, (1980).
- Flaman, A.A.M., Dijksman, J.F.: "Non-Isothermal and Transient Flow of Molten Polymer in an Open Tectangular Cavity", Proceedings of the Eight International Heat Transfer Conference, San Fransisco, (1986) 1751-1754.
- Gutfinger, C., Broyer, E., Tadmor, Z.: "Melt Solidification in Polymer Processing", Polym. Eng. and Sci., 15(7) (1975) 515-524.
- Hieber, C.A., Shen, S.F.: "A Finite-Element/Finite-Difference Simulation of the Injection-Molding Filling Process", J. of Non-Newt. Fluid. Mech., 7 (1980) 1-32.
- Hieber, C.A., Socha, L.S., Shen, S.F., Wang, K.K., Isayer, A.I.: "Filling Thin Cavities of Variable Gap Thickness: A Numerical and Experimental Investigation", Polym. Eng. and Sci., 23(1) (1983) 20-26.
- Hill, J.M.: "One-dimensional Stefan problems", Harlow, (1987).
- Iizuka, K., Gotoh, T., Miyamoto, M., Kubo, N., Osaka, M., Sahara, K.: "A simulation system for injection molding process", Proceedings of the NUMIFORM '86 Conference, Gothenburg, (1986).
- Janeschitz-Kriegl, H.: "Injection moulding of plastics. Some idea about the relation between mould filling and birefringence", Rheol. Acta, 16 (1977) 327-339.
- Janeschitz-Kriegl, H.: "Injection moulding of plastics II. Analytical solution of heat transfer problem", Rheol. Acta, 18 (1979) 693-701.
- Janeschitz-Kriegl, H.: "Polymer Melt Rheology and Flow Birefringence", Springer (1983).
- Janeschitz-Kriegl, H., Krobath, G., Roth, W., Schausberger, A.: "On the Kinetics of Polymer Crystallization under shear", Eur. Polym. J., 19(10/11) (1983) 983-898.
- Janeschitz-Kriegl, H., Eder, G., Krobath, G., Liedauer, S.: "The Stefan Problem in Polymer Processing: Theory and Experimentation", J. of Non-Newt. Fluid Mech., 23 (1987) 107-122.
- Janeschitz-Kriegl, H., Wimberger-Friedl, R., Krobath, G., Liedauer, S.: "Uber die Ausbildung von Schichtstrukturen in Kunststoff-Formteilen", Kunststoffe, 40(4) (1987) 301-307.

- "Kenndaten für die Verarbeitung thermoplastischer Kunststoffe: I. Thermodynamik", Hanser, München; Wien, (1979).
- "Kenndaten für die Verarbeitung thermoplastischer Kunststoffe: II. Rheologie", Hanser, München; Wien, (1982).
- Kersemakers, J., Internal Report DSM, (1987).
- Knappe, W.: "Die thermischen Eigenschaften von Kunststoffe", Kunststoffe, 66(5) (1976) 297-302.
- Krueger, W.L., Tadmor, Z.: "Injection Modling into a Rectangular Cavity with Inserts", Polym. Eng. and Sci., 20(6) (1980) 426-431.
- Lapidus, L., Pinder, G.F.: "Numerical Solution of Partial Differential Equations in Science and Engineering", Wiley, New York, (1982).
- Latrobe, A., De la Lande, M.E., Bung, H.: "Numerical Simulation of Mold Filling with Polymers", preprint.
- Laurencena, B.R., Williams, C.: "Radial Flow of Non-Newtonian Fluids Between Parallel Plates", Trans. of the Soc. of Rheol., 18(3) (1974) 331-355.
- Lord, H.A., Williams, G.: "Mold-filling Studies for the Injection Molding of Thermoplastic Materials. Part II: The Transient Flow of Plastic Materials in the Cavities of Injection-Molding Dies", Polym. Eng. and Sci., 15(8) (1975) 569-582.
- Malvern, L.E.: "Introduction to the mechanics of a continuous medium", Prentice-Hall, (1969).
- Martin, B.: "Some analytical solutions for viscometric flows of Power-law fluids with heat generation and temperature dependent viscosity", Int. J. Non-linear Mech., 2 (1967) 285-301.
- Mavridis, H., Hrymak, A.N., Vlachopoulos, J.: "Finite Element Simulation of Fountain Flow in Injection Molding", Polym. Eng. and Sci., 26(7) (1986) 449-454.
- Mhaskar, R.D., Shah, Y.T., Pearson, J.R.A.: "On the Stability of Flow in Channels with a Moving Boundary: The Mold Filling Problem", Trans. of the Soc. of Rheol., 21(2) (1977) 291-300.
- Müller, I.: "Thermodynamics", Mid-County Press, London, (1985).
- Ockendon, H., Ockendon, J.R.: "Variable-viscosity flows in heated and cooled channels", J. Fluid Mech., 83(1) (1977) 177-190.

- Ockendon, H.: "Channel flow with temperature-dependent viscosity and internal viscous dissipation", J. Fluid Mech., 93(4) (1979) 737-746.
- Pearson, J.R.A., Shah, Y.T.: "On the stability of non-isothermal flow in channels", Rheol. Acta 12 (1973) 240-244.
- Pearson, J.R.A., Shah, Y.T., Vieira, E.S.A.: "Stability of non-isothermal flow in channels - I. Temperature-dependent Newtonian fluid without heat generation", Ch. Eng. Sci., 28 (1973) 2079-2088.
- Pearson, J.R.A.: "Variable-viscosity flows in channels with high heat generation", J. Fluid Mech., 83(1) (1977) 191-206.
- Pearson, J.R.A., Richardson, S.M.: "Computational analysis of polymer processing", Appl. Sci. Publ. Ltd, (1983).
- Pearson, J.R.A.: "Mechanics of Polymer Processing", Elsevier, (1985).
- Richardson, S.: "Hele Shaw flows with a free boundary produced by the injection of fluid into a narrow channel", J. Fluid Mech. 56(4) (1972) 609-618.
- Richardson, S.M., Pearson, H.J., Pearson, J.R.A.: "Simulation of Injection Moulding", Plastic and Rubber Processing, 5 (1980) 55-65.
- Richardson, S.M.: "Injection moulding of thermoplastics. I. Freezing-off at gates", Rheol. Acta, 24 (1985) 497-508.
- Richardson, S.M.: "Injection moulding of thermoplastics. II. Freezing-off in cavities", Rheol. Acta, 24 (1985) 509-518.
- Richardson, S.M.: "Injection moulding of thermoplastics: Freezing of variable-viscosity fluids. I. Developing flows with very high heat generation", Rheol. Acta, 25 (1986) 180-190.
- Richardson, S.M.: "Injection moulding of thermoplastics: Freezing of variable-viscosity fluids. II. Developing flows with very low heat generation", Rheol. Acta, 25 (1986) 308-318.
- Richardson, S.M.: "Injection moulding of thermoplastics: Freezing of variable-viscosity fluids. III. Fully-developed flows", Rheol. Acta, 25 (1986) 372-379.
- Schlichting, H.: "Grenzschicht-Theorie", Braun, Karlsruhe, (1982).
- Schmidt, L.R.: "Hele-Shaw Flow of Polypropylene past a Circular Cylinder", Proceedings of the VIIth International Congress on Rheology, Gothenburg, Sweden (1976).

- Shah, Y.T., Pearson, J.R.A.: "Stability of non-isothermal flow in
  channels - II. Temperature-dependent power-law fluids without heat
  generation", Ch. Eng. Sci., 29 (1974) 737-746.
- Shah, Y.T., Pearson, J.R.A.: "Stability of non-isothermal flow in
  channels - III. Temperature-dependent power-law fluids with heat
  generation", Ch. Eng. Sci., 29 (1974) 1485-1493.
- Shen, S.F.: "Polymer-flow modelling and simulation of the
  injection-molding process", Proceedings of the NUMIFORM '86 Confer-
  ence, Gothenburg, (1986).
- Sitters, C.W.M., Dijksman, J.F.: "On the Mathematical Modelling of
  the Injection Moulding Process", Integration of Fundamental Polymer
  Science and Technology, Elsevier, London; New York (1986).
- Stevenson, J.F., Galskoy, A., Wang, K.K., Chen, I., Reber, D.H.:
  "Injection MOlding in Disk-Shaped Cavities", Polym. Eng. and Sci.,
  17(9) (1977) 706-710.
- Tadmor, Z.: "Molecular Orientation in Injection Molding", J. of
  Appl. Polym. Sci., 18 (1974) 1753-1772.
- Vanderschuren, L., Dupret, F.: "Three-dimensional calculation of
  the temperature field during injection molding", Proceedings of the
  NUMIFORM '86 Conference, Gothenburg, (1986) 199-204.
- Valstar, J.M., Beek, W.J.: "Warmteoverdracht naar een laminaire
  stroming van een niet-Newtonse vloeistof tussen twee evenwijdige
  platen", De Ingeneiur, 75 (1963) Ch. 1-7.
- Wales, J.L.S., Van Leeuwen, J., Van der Vijgh, R.: "Some Aspects of
  Orientation in Injection Molded Objects", Polym. Eng. and Sci., 12
  (1972) 358-363.
- Wales, J.L.S.: "The application of flow birefringence to rheologi-
  cal studies of polymer melts", University Press, Delft, (1976).
- White, J.L.: "Fluid Mechanical Analysis of Injection Mold Filling",
  Polym. Eng. and Sci., 15(1) (1975) 44-50.
- White, J.L., Dietz, W.: "Some Relationships Between Injection
  Molding Conditions and the Characteristics of Vitrified Molded
  Parts", Polm. Eng. and Sci. 19(15) (1979) 1081-1091.
- Wijngaarden, H. van, Dijksman, J.F.: "Non-Isothermal Flow of a
  Molten Polymer in a Narrow Rectangular Cavity", J. of Non-Newt.
  Fluid Mech., 11 (1982) 175-199.

- Williams, G., Lord, H.A.: "Mold-Filling Studies for the Injection Molding of Thermoplastic Materials. part I: The Flow of Plastic Materials in Hot- Cold-Walled Circular Channels", Polym. Eng. and Sci., 15(8) (1975) 553-568.
- Zienkiewicz, O.C.: "The finite element method", McGraw-Hill, (1977).

Samenvatting

Spuitgieten van thermoplastische materialen is een industrieel pro-
ces, voor het in grote aantallen en tegen geringe kosten vervaardigen
van complexe dunwandige producten in één machine cyclus. Niet in de
laatste plaats als gevolg van de ontwikkeling van nieuwe polymeren
met een superieure kwaliteit, worden de eisen die aan producten ge-
steld worden steeds hoger. Ook groeit het aantal toepassingen ten
nadele van conventionele productietechnieken. Om het gebrek aan erva-
ring in deze gebieden enigszins te compenseren is het gewenst nume-
riek gereedschap te ontwikkelen, om de invloed van de belangrijkste
materiaalparameters en procescondities op de uiteindelijke product-
kwaliteit te kunnen voorspellen. Vanuit fysisch oogpunt gezien is het
spuitgietproces zeer complex. Dit onderzoek beperkt zich tot het in-
jecteren van een polymere vloeistof in een complex gevormde matrijs-
holte, met variërende geringe spleethoogte. Door de (asymmetrische)
koeling van de matrijs, zullen vanaf de wanden gestolde lagen
groeien. De viscositeit van het polymeer is afhankelijk van de
temperatuur, de afschuifsnelheid en de druk. Het specifiek volume en
de overige thermodynamische grootheden zijn temperatuur- en
drukafhankelijk.
Dit onderzoek bevat een aantal nieuwe aspecten. De mathematische ba-
sis wordt gevormd door een algemene continuüms formulering, waarbij
de scheiding tussen vaste stof en vloeistof wordt beschreven door een
discontinuïteitsvlak. In alle richtingen wordt warmteconvectie in
rekening gebracht. Een stabiele expliciete methode is ontwikkeld om
het vloeifront te bepalen in elke willekeurige complexe configuratie.
Een aantal numerieke simulaties wordt behandeld en vergeleken met
experimentele waarnemingen en numerieke resultaten uit de literatuur.
De methode ter bepaling van het vloeifront werkt bevredigend. Dit
geldt ook voor de bepaling van de druk- en het temperatuurveld. Hier-
bij dient echter opgemerkt te worden dat voor de gepresenteerde re-
sultaten, de snelheidscomponent in de richting van de kanaalhoogte
niet verdisconteerd is. De reden hiervan is dat voor deze snelheids-
component slechts onvoldoend betrouwbare waarden berekend konden wor-
den. Een ander probleem is de afnemende kwaliteit van de resultaten
voor het temperatuurveld bij toenemende injectietijd. Een voorstel

wordt gedaan om deze tekortkomingen op te heffen. Desalniettemin ver-
schaft het gepresenteerde werk de mogelijkheid om het gedrag van po-
lymeren tijdens de injectiefase van het spuitgietproces op verbeterde
wijze te voorspellen.

Curriculum vitae

13 november 1953	Geboren te Klundert
1966-1971	H.B.S. te Oudenbosch
1971-1975	H.T.S. te Dordrecht
1975-1976	Militaire dienst
1976-1983	Technische Hogeschool Eindhoven
	Afdeling Werktuigbouwkunde
1983-1984	Wetenschappelijk medewerker van het Philips
	Natuurkundig Laboratorium te Eindhoven
1984-	Universitair docent aan de Technische Universiteit
	Eindhoven, Faculteit Werktuigbouwkunde, vakgroep
	Fundamentele Werktuigbouwkunde

STELLINGEN

behorende bij het proefschrift
NUMERICAL SIMULATION OF INJECTION MOULDING
van Cox Sitters

1. De beschrijving van het stolgedrag van semi-kristallijne
    polymeren vereist discontinuïteitsvlakken bij de (uitwerking
    van de) balanswetten.
    - Dit proefschrift, H2.

2. Op basis van numerieke analyses moet het mogelijk zijn een
    betere analytische benadering van de stroming aan het
    vloeifront af te leiden. Een isotherme oplossing voor dit
    probleem is reeds aanwezig.
    - H. Mavridis, A.N. Hrymak en J. Vlachopoulos, Polym. Eng. and
      Sci., 26 (7) (1987) 449-454.

3. Om tot een betere numerieke oplossing van het spuitgietproces
    te komen is het vooral belangrijk om elementen te formuleren
    die continuïteit van de drukgradient waarborgen. Het toepassen
    van hogere orde elementen is minder belangrijk.
    - Dit proefschrift, H5 en H6.

4. Het is van eminent belang een sensor te ontwikkelen, waarmee de
    temperatuurverdeling in plaats en tijd tijdens het spuitgiet-
    proces vastgelegd kan worden.

5. Hieber en Shen kunnen door een kleine aanpassing bij de nume-
    rieke bepaling van de optredende drukken tijdens het spuitgiet-
    proces, de convergentiesnelheid van het niet-lineaire Poisson
    probleem drastisch opvoeren.
    - C.A. Hieber en S.F. Shen, J. of Non-Newt. Fluid Mech., 7
      (1980) 1-32.

6. Het verdient aanbeveling de klassieke beschrijving van het stollingsproces van semi-kristallijne polymeren te vervangen door een werkwijze, waarbij de kristallisatiesnelheid een functie is van de temperatuur.
   - G. Eder en H. Janeschitz-Kriegl, Polymer Bulletin, 11 (1984) 93-98.
   - H. Janeschitz-Kriegl, G. Eder, G. Krobath en S. Liedauer, J. of Non-Newt. Fluid Mech., 23 (1987) 107-122.

7. In tegenstelling tot de gerapporteerde bevindingen van Hieber en Shen werkt de in dit proefschrift gehanteerde "straight forward procedure" om het vloeifront te bepalen bevredigend: er ontwikkelt zich geen oscillerend vloeifront.
   - C.A. Hieber en S.F. Shen, J. of Non-Newt. Fluid Mech., 7 (1980) 1-32.
   - Dit proefschrift, H5.

8. Het heeft weinig zin door te gaan met de ontwikkeling van nume- riek gereedschap voor de simulatie van het spuitgietproces in- dien de experimentele bepaling van materiaaleigenschappen niet verbeterd en uitgebreid wordt. De computersimulaties zijn zeer nuttig om via "gevoeligheidsanalyses" de experimenten te sturen.
   - Dit proefschrift, H4 en H6.3.

9. De door Schoofs ontwikkelde optimaliseringsmethode kan succesvol gebruikt worden bij het ontwerp van een "packaging" van IC's.
   - A.J.G. Schoofs, Dissertatie Technische Universiteit Eindhoven, (1987).

10. Het is alleszins redelijk dat studenten in de technische wetenschappen zelf beschikken over een kleine computer.